

# Probing the southern African lithosphere with magnetotellurics, Part II, linking electrical conductivity, composition and tectono-magmatic evolution.

Özaydin Sinan<sup>1</sup>, Selway Kate<sup>2</sup>, Griffin William L<sup>3</sup>, and Moorkamp Max<sup>4</sup>

<sup>1</sup>Macquarie University

<sup>2</sup>Future Industries Institute, University of South Australia

<sup>3</sup>Arc Centre of Excellence for Core to Crust Fluid Systems and GEMOC ARC National Key Centre

<sup>4</sup>Ludwig Maximilians Universitaet

November 16, 2022

## Abstract

The tectonic history of Southern Africa includes Archean formation of cratons, multiple episodes of subduction and rifting and some of the world's most significant magmatic events. These processes left behind a compositional trail that can be observed in xenoliths and measured by geophysical methods. The abundance of kimberlites in southern Africa makes it an ideal place to test and calibrate mantle geophysical interpretations that can then be applied to less well-constrained regions. Magnetotellurics (MT) is a particularly useful tool for understanding tectonic history because electrical conductivity is sensitive to temperature, bulk composition, accessory minerals and rock fabric. We produced three-dimensional MT models of the southern African mantle taken from the SAMTEX MT dataset, mapped the properties of  $\sim 36000$  garnet xenocrysts from Group I kimberlites, and compared the results. We found that depleted regions of the mantle are uniformly associated with high electrical resistivities. The conductivity of fertile regions is more complex and depends on the specific tectonic and metasomatic history of the region, including the compositions of metasomatic fluids or melts and the emplacement of metasomatic minerals. The mantle beneath the  $\sim 2.05$  Ga Bushveld Complex is highly conductive, probably caused by magmas flowing along a lithospheric weakness zone and precipitating interconnected, conductive accessory minerals such as graphite and sulfides. Kimberlites tend to be emplaced near the edges of the cratons where the mantle below 100 km depth is not highly resistive. Kimberlites avoid strong mantle conductors, suggesting a systematic relationship between their emplacement and mantle composition.

1                   **Probing the southern African lithosphere with**  
2                   **magnetotellurics, Part II, linking electrical**  
3                   **conductivity, composition and tectono-magmatic**  
4                   **evolution.**

5                   **Sinan Özaydın<sup>1</sup>, Kate Selway<sup>2,1</sup>, William L. Griffin<sup>1</sup>, Max Moorkamp<sup>3</sup>**

6                   <sup>1</sup>Macquarie University, ARC Centre of Excellence for Core to Crust Fluid Systems (CCFS), Department  
7                   of Earth and Environmental Sciences, Sydney, Australia

8                   <sup>2</sup>University of South Australia, Future Industries Institute, Adelaide, Australia

9                   <sup>3</sup>Ludwig-Maximilians-Universität, Department of Earth and Environmental Sciences, Munich, Germany

10                   **Key Points:**

- 11                   • Comprehensive comparison of 3D magnetotelluric models and composition from  
12                   garnet xenocrysts are carried out in southern Africa.  
13                   • Depleted regions are associated with resistors, whereas the conductivity of fertile  
14                   regions depends on the style of metasomatism.  
15                   • Kimberlites tend to be around the resistors while avoiding the conductors, sug-  
16                   gesting an interplay between mantle composition and magmatism.

---

Corresponding author: Sinan Özaydın, [sinan.ozaydin@protonmail.com](mailto:sinan.ozaydin@protonmail.com)

## Abstract

The tectonic history of Southern Africa includes Archean formation of cratons, multiple episodes of subduction and rifting and some of the world's most significant magmatic events. These processes left behind a compositional trail that can be observed in xenoliths and measured by geophysical methods. The abundance of kimberlites in southern Africa makes it an ideal place to test and calibrate mantle geophysical interpretations that can then be applied to less well-constrained regions. Magnetotellurics (MT) is a particularly useful tool for understanding tectonic history because electrical conductivity is sensitive to temperature, bulk composition, accessory minerals and rock fabric. We produced three-dimensional MT models of the southern African mantle taken from the SAMTEX MT dataset, mapped the properties of  $\sim 36000$  garnet xenocrysts from Group I kimberlites, and compared the results. We found that depleted regions of the mantle are uniformly associated with high electrical resistivities. The conductivity of fertile regions is more complex and depends on the specific tectonic and metasomatic history of the region, including the compositions of metasomatic fluids or melts and the emplacement of metasomatic minerals. The mantle beneath the  $\sim 2.05$  Ga Bushveld Complex is highly conductive, probably caused by magmas flowing along a lithospheric weakness zone and precipitating interconnected, conductive accessory minerals such as graphite and sulfides. Kimberlites tend to be emplaced near the edges of the cratons where the mantle below 100 km depth is not highly resistive. Kimberlites avoid strong mantle conductors, suggesting a systematic relationship between their emplacement and mantle composition.

## Plain Language Summary

The present-day composition of Earth's tectonic plates results from past geological processes. We can learn about Earth's composition from deep rock samples that are carried to the surface during volcanic eruptions and by probing its physical properties, like electrical conductivity, with geophysics. In southern Africa, there are extensive deep rock samples, which have been brought to the surface by kimberlite volcanoes that also host diamonds, and also extensive geophysical data. In this paper, we compare the rock compositions with electrical conductivity to learn more about Earth's composition. Our results show that the oldest parts of the plates that retain compositions similar to their initial composition appear resistive. On the other hand, regions that have been intruded by deep fluids or molten rock can be resistive or conductive, depending on the types of minerals that were formed during the intrusion. The kimberlite volcanoes mostly erupted through the edges of the most resistive parts of the plates and did not erupt through the conductors. These results will help us to make more accurate interpretations about the composition of parts of the Earth where we do not have deep rock samples.

## 1 Introduction

The Kalahari Craton in southern Africa is an assemblage of Archean and Proterozoic tectonic terranes (De Wit et al., 1992; Jacobs et al., 2008). During three billion years of plate reorganisation, numerous tectono-magmatic events have influenced its compositional structure (e.g., Hanson et al., 2006; Beukes et al., 2019) and are evident not only in surface geology and potential field geophysical data (Corner & Durrheim, 2018) but also in large lateral variations in the state of the mantle inferred from seismic tomography (e.g., Ortiz et al., 2019; White-Gaynor et al., 2020; Fouch et al., 2004; Yang et al., 2008) and magnetotelluric studies (e.g., Evans et al., 2011; Khoza et al., 2013a, 2013b). Due to the presence of extensive outcropping rocks and mantle xenolith-bearing kimberlites (e.g., Griffin et al., 2003; Jelsma et al., 2004), the Kalahari Craton is a great natural laboratory to understand craton formation and survival as well as plate tectonic and magmatic processes throughout geological time. These rocks and xenoliths indicate that

67 the Kalahari Craton mantle composition is highly variable (e.g., Griffin et al., 2003; Hum-  
68 bert et al., 2019). Variations in mantle composition are either a result of the age-dependent  
69 thermal state and composition of the mantle as it initially formed (e.g., Griffin et al., 1999;  
70 Pearson et al., 2004) or subsequent alterations imposed by melts and fluids that infil-  
71 trated the lithospheric mantle (Alard et al., 2000; Griffin et al., 2003). The Kalahari Cra-  
72 ton and its surroundings also hold crucial economic deposits such as the PGE-rich lay-  
73 ers of the Bushveld Complex (VanTongeren, 2017) and diamond-bearing kimberlites (Jelsma  
74 et al., 2004; A. G. Jones et al., 2009), which formed as the result of lithospheric-scale pro-  
75 cesses (Begg et al., 2010; Griffin et al., 2013). Therefore, studying lithospheric compo-  
76 sition may improve models for economic geology as well as continental evolution.

77 The magnetotelluric (MT) method is a geophysical technique that images the sub-  
78 surface electrical conductivity structure of the Earth to upper mantle depths. Electri-  
79 cal conductivity can provide knowledge on bulk composition and temperature as well as  
80 the presence of interconnected accessory materials (e.g., fluids, melt, hydrous minerals  
81 and sulphides). Previous studies have shown that the cratonic mantle has highly vari-  
82 able electrical conductivity that cannot be accounted for by temperature differences alone  
83 (e.g., Selway, 2015; Evans et al., 2011). These conductivity variations can partly be as-  
84 cribed to hydrogen species structurally bound to the nominally anhydrous minerals (NAMs)  
85 that constitute the bulk of the upper mantle, such as olivine, pyroxenes, garnet and spinel  
86 (Demouchy & Bolfan-Casanova, 2016).

87 In this article, we investigate the relationships between the Kalahari Craton’s tec-  
88 tonic setting, thermal structure, magmatic events and metasomatic signatures with its  
89 geoelectric structure. We use the continental-scale South African Magnetotelluric Ex-  
90 periment (SAMTEX) dataset (A. G. Jones et al., 2009) to produce 3D MT models of  
91 the mantle, and we estimate the composition, metasomatic signatures and thermal struc-  
92 ture from analyses made on 36066 garnet xenocrysts taken from southern African kim-  
93 berlites. This article represents the second part of a two-part study. In the first part (Moorkamp  
94 et al., 2021), we investigated 3D MT modelling of the SAMTEX dataset using different  
95 inversion algorithms (Kelbert et al., 2014; Moorkamp et al., 2011) and aimed to under-  
96 stand the effects of strategies used to model the mantle conductivities. In this paper, we  
97 rely mainly on the inversion of the “selected data” dataset run with *ModEM* from a me-  
98 dian starting model described in that work, while being mindful of the robustness of these  
99 features implied by different modelling attempts. We refer any reader that is interested  
100 in the MT modelling aspect of this study to the first part (Moorkamp et al., 2021).

## 101 **2 Tectonic evolution of the Kalahari Craton and surrounding terranes**

102 The Kalahari Craton consists of terranes with Archean to Neoproterozoic basement  
103 ages, namely the Zimbabwe Craton, Kaapvaal Craton, Limpopo Belt, Kheis Belt, Magondi  
104 Belt and Rehoboth Terrane (Figure 1). Many of the older basement terranes are hid-  
105 den under the cover of Neogene Kalahari Group sediments and thick marine-sedimentary  
106 sequences of the Jurassic Karoo Group. Due to this cover, most geological understand-  
107 ing of Botswana and the Rehoboth Terrane is derived from geophysical and borehole data  
108 (e.g., Chisenga et al., 2020; Corner & Durrheim, 2018). In contrast, the basement rocks  
109 of the Kaapvaal and Zimbabwe cratonic nuclei and their immediate surrounding blocks  
110 in the eastern Kalahari Craton are better exposed (Figure 1) and have been the subject  
111 of rigorous geological and geophysical study for many decades (Oriolo & Becker, 2018;  
112 Corner & Durrheim, 2018; De Beer, 2016).

113 The basement of the Kaapvaal Craton is dominated by 3.6-2.9 Ga gneiss, grani-  
114 toid and greenstone belts (Poujol et al., 2003). The orientations of the greenstone belts  
115 are markedly different in the Kimberley Block in the western Kaapvaal Craton and the  
116 Witwatersrand Block in the eastern Kaapvaal Craton, separated by the Colesburg Mag-  
117 netic Lineament (Figure 1), which suggests the independent formation of these Archean

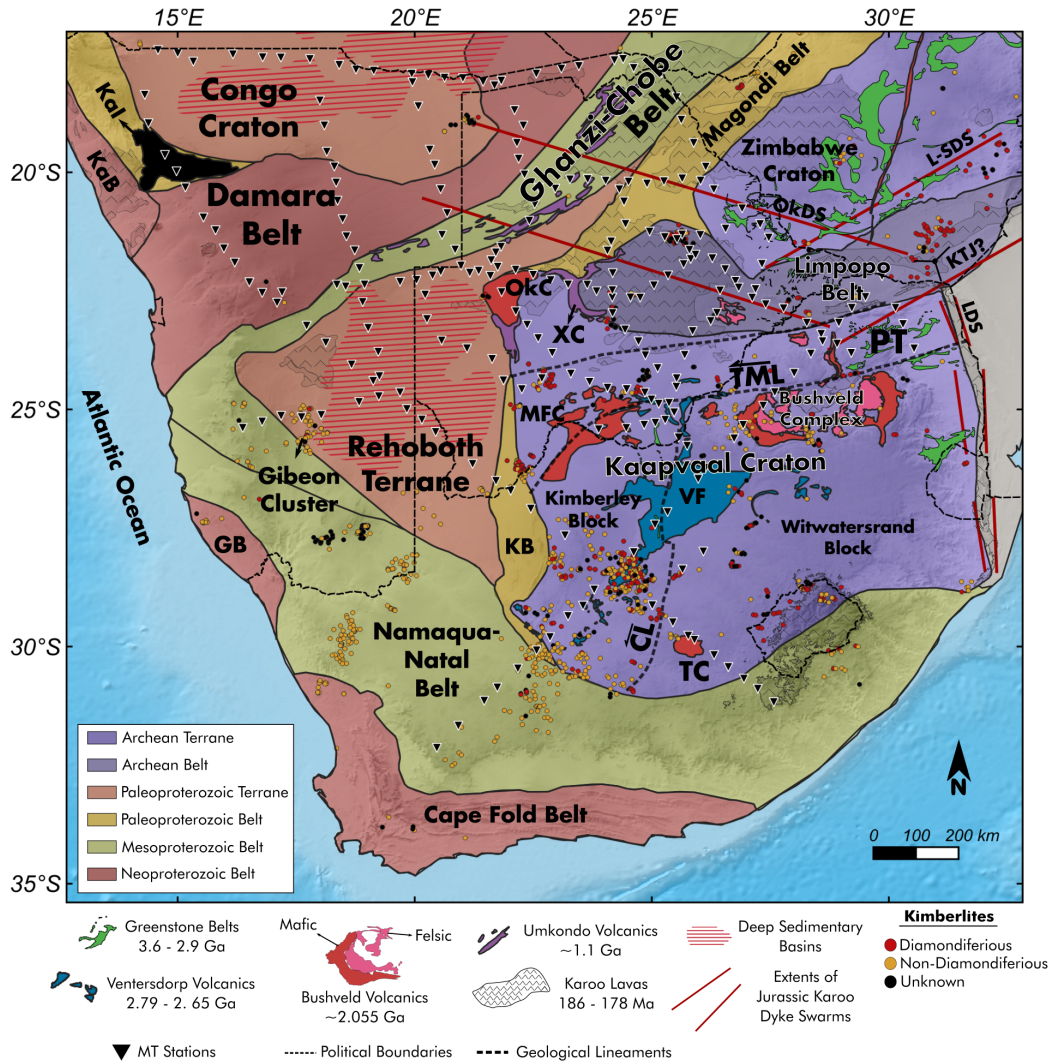


**Figure 1.** Map featuring the tectonic units of Southern Africa, including greenstone belts and major igneous formations. CL: Colesburg Lineament, GB: Gariiep Belt, KB: Kheis Belt, KaB: Kaoka Belt, KaI: Kamanjab Inlier, KTJ: Karoo Triple Junction, LDS: Lebombo Dyke Swarm, L-SDS: Limpopo-Save Dyke Swarm, MFC: Molopo-Farms Complex, OkC: Okwa Complex, OkDS: Okavango Dyke Swarm, PT: Pietersburg Terrane, TC: Trompsburg Complex, TML: Thabazimbi-Murchison Lineament, XC: Xade Complex, VF: Ventersdorp Formation. Data compiled from several studies (McCourt et al., 2013; Hanson, 2003; Corner & Durrheim, 2018; Chisenga et al., 2020)

118 terranes before amalgamation into a single craton (Jacobs et al., 2008). In the north-  
119 ern Kaapvaal Craton, the Pietersburg Terrane is thought to have accreted to the Wit-  
120 watersrand Block at 2.73 - 2.65 Ga (Laurent et al., 2019). This collision created the Thabazimbi-  
121 Murchison Lineament (TML), a trans-lithospheric structure observed in aeromagnetic  
122 data (Good & De Wit, 1997). Assembly of the Kaapvaal Craton was accompanied by  
123 the formation of the foreland Witwatersrand Basin (3.0 - 2.78 Ga), the rift-related Ven-  
124 tersdorp Volcanic Sequence (2.79 - 2.65 Ga, Gumsley et al., 2020) and deposition of Transvaal  
125 Supergroup (2.6 - 2.058 Ga, Zeh et al., 2020). The final amalgamation of the Pieters-  
126 burg Terrane with the Witwatersrand Block occurred during the collision between the  
127 Kaapvaal Craton and the Zimbabwe Craton to the north. The Limpopo microcontinent  
128 was wedged between the two cratons during this collision (2.71-2.67 Ga, Laurent et al.,  
129 2019), giving rise to the Limpopo Orogeny and the formation of the Limpopo Belt.

130 Accretion of the Paleoproterozoic belts and blocks started around 2.06 Ga, corre-  
131 sponding to the timing of the Bushveld and syn-Bushveld magmatism along the TML  
132 (Molopo Farms Complex, Okwa Complex, Zeh et al., 2015) and amalgamation of Archean  
133 terranes (Laurent et al., 2019; Oriolo & Becker, 2018). The Magondi Belt accreted onto  
134 the northwestern end of the Zimbabwe Craton through subduction processes (Master et  
135 al., 2010; Jacobs et al., 2008) and then experienced coeval transpressional deformation  
136 and metamorphism with the Limpopo Block in response to a collision with an unknown  
137 terrane from northwest (Oriolo & Becker, 2018). Contemporaneously, the western end  
138 of the Kaapvaal Craton experienced sedimentation of Kheis Belt units and subsequent  
139 collision with the Rehoboth Terrane (Jacobs et al., 2008) along the prominent Kalahari  
140 Magnetic Lineament (Corner & Durrheim, 2018). The tectonic history and basement ge-  
141 ology of the Rehoboth Terrane are somewhat enigmatic due to the thick sedimentary se-  
142 quences covering the surface, especially in the central region. Geochemical and geochrono-  
143 logical data from the westernmost inliers suggest that the Rehoboth Terrane formed and  
144 accreted onto the Kaapvaal Craton and Kheis Belt in a convergent-arc setting at 1.77  
145 -1.72 Ga (Van Schijndel et al., 2014).

146 Following the Paleoproterozoic evolution and cratonisation of the region, by the  
147 Mesoproterozoic the assembled Kaapvaal-Limpopo-Zimbabwe-Rehoboth Block was be-  
148 having as a rigid block (Jacobs et al., 2008). After stabilisation, the region was impacted  
149 by 1.4-1.35 Ga intraplate alkaline magmatism (Pilanesberg Complex and Premier kim-  
150 berlite Hanson et al., 2006). This was followed by the more abundant and widespread  
151 magmatism concentrated near the northwestern border of the craton associated with the  
152  $\sim 1.1$  Ga Umkondo Large Igneous Province, an event thought to be related to rifting  
153 (De Kock et al., 2014; Hanson et al., 2006) that used the lithospheric-scale weakness zones  
154 formed during assembly of the proto-Kalahari Craton (e.g., Xade Complex, Hanson et  
155 al., 2006). The Umkondo-aged rhyolitic units (Kgwebe Formation and southwestern cor-  
156 relatives) mostly outcrop along a ridge in the Ghanzi-Chobe Belt stretching from north-  
157 eastern Botswana to central Namibia. This ridge was uplifted in response to the Neo-  
158 proterozoic Pan-African Orogeny, which also formed the Damara Belt (Modie, 2000). To  
159 the south, the Kalahari Craton is bounded by the Proterozoic Namaqua-Natal Belt, which  
160 formed as an assemblage of numerous microcontinental terranes in a convergent setting.  
161 The Namaqua-Natal Belt collided with and accreted onto the Kalahari Craton during  
162 series of tectonic events between 1.2 - 1.0 Ga (Jacobs et al., 2008).

163 The Jurassic breakup of Gondwana had a significant impact on the Kalahari Cra-  
164 ton, including the emplacement of widespread rift-related Karoo units (e.g., Drakens-  
165 berg Lavas, Karoo diorite sills, Okavango and Save-Limpopo Dyke Swarms, Svensen et  
166 al., 2012). Following the Karoo event, extensive Group II ( $\sim 110$ – $127$  Ma) and Group  
167 I ( $\sim 110$  –  $72$  Ma) kimberlites were emplaced in the Kalahari Craton. Differences in  
168 mantle xenolith and xenocryst compositions between kimberlites from these two time  
169 windows indicate an intervening major metasomatic event in the mantle (Kobussen et  
170 al., 2009).

### 3 Methods

#### 3.1 Garnet xenocryst analyses

Analyses were carried out on existing data collected from 36066 garnet xenocryst samples taken from Group I kimberlites around Southern Africa (Table S1). The data include major-element analyses by electron microprobe and trace-element data collected using with laser-ablation ICPMS techniques, in both the GEMOC ARC National Key Centre, Macquarie University and the DeBeers Group Services Laboratory, Johannesburg, South Africa (Kobussen et al., 2008, 2009). To make depth-dependent classifications, we first performed thermobarometry on these samples. Our methodology in estimating pressure and temperature follows the steps: (1) Calculating  $P_{Cr}^{max}$ - $T_{Ni}$  conditions with nickel-in-garnet thermometry and the chromium solubility barometer of Ryan et al. (1996). (2) Fitting a generalized cratonic geotherm of Hasterok & Chapman (2011) based on the locus of maximum  $P_{Cr}$  at each  $T_{Ni}$ . (3) Defining the temperature at the base of the depleted lithosphere ( $T_{BDL}$ ) as the temperature at which the proportion of garnets with  $\leq 10$  ppm (wt) yttrium decreases sharply. (4) Finding the intersection point of the selected conductive geotherm with the  $T_{BDL}$  value to obtain the thickness of the depleted lithosphere. (5) Defining the so-called kinked geotherm above  $T_{BDL}$  as a line parallel to the diamond-graphite transition (Day, 2012). (6) Finally, projecting the temperatures of garnet samples to the defined geotherm to determine their depth of origin. The calculated geotherm parameters for each pipe are given in Tables S1 and S2, and fitted generalized cratonic geotherm surface heat flow (SHF) values are mapped in Figure 5b.

For the garnet xenocryst classifications depicted in Figures 5 and 6, we used the method of cluster analysis by regressive partitioning (CARP, Griffin et al., 2002). This method classifies Cr-pyrope garnets into statistically significant populations of similar trace- and major-element compositions that define lithology and metasomatic signatures. For the purpose of this work the CARP classes are combined into five main groups: (1) depleted harzburgites, (2) depleted lherzolites, (3) depleted lherzolites with phlogopite metasomatism, (4) fertile lherzolites and (5) melt-metasomatised. Depleted harzburgites and lherzolites (yellow, Figures 5 and 6) represent mantle rocks that have experienced only minor metasomatism since their formation. They are depleted in terms of major- and trace-elements and their garnets show sinuous  $REE_N$  patterns (Figure S48-S50), which Griffin et al. (1999) suggested to be a feature related to specific Archean metasomatic processes. Depleted lherzolites with phlogopite metasomatism (blue) have relatively depleted major element compositions but trace-element (Ti, Zr) signatures characteristic of phlogopite crystallisation. The most populous metasomatic class, fertile lherzolites (green), represents rocks with compositions enriched in major and trace elements with more diverse characteristics. These could be rocks that never experienced depletion, or depleted Archean material that was later refertilised. While depleted and refertilised signatures are usually associated with the Archean mantle, signatures of the mantle that has never been depleted are usually associated with Proterozoic or younger mantle (Griffin et al., 2002). Samples from the “melt-metasomatised” class (red) are associated with very enriched, high temperature lherzolites. They commonly show sheared microstructures which indicate melt infiltration into the rock (Griffin et al., 2003) and are largely located below the base of the depleted lithosphere. Whole-rock  $Al_2O_3$  contents used in Figure 5a are calculated from regression analyses made on yttrium-in-garnet (O’Reilly & Griffin, 2006), while  $Mg^{ol}\#$  is calculated from the garnet data by the method described in Gaul et al. (2000).

$REE_N$  patterns of the CARP classes mostly demonstrate significantly different characteristics. The sinuosity of the REE patterns is associated with depleted material in the mantle (Griffin et al., 1999) and can be quantified by using the  $\log-Nd_N/Dy_N$  ratio, in which values above zero indicate sinuous patterns and values below zero indicate less sinuous patterns.  $Yb_N$ , on the other hand, is used as a proxy of overall HREE enrichment.

224 Metasomatic CARP classes exhibit less sinuous patterns, heavy REE (HREE) enrich-  
 225 ment and light REE (LREE) depletion. During refertilisation, garnet  $REE_N$  trends be-  
 226 come less sinuous (lower  $\log-Nd_N$   $Dy_N$ ), with higher  $HREE_N/LREE_N$  ratios, as the  
 227 metasomatic fluids percolate more extensively and equilibrate with the environment (Grif-  
 228 fin et al., 2003). When the mean values of  $\log-Nd_N$   $Dy_N$  and  $Yb_N$  are plotted against  
 229 depth (Figure 8b,c), they are correlated (negatively and positively, respectively) with the  
 230 population of total metasomatic classes within the fertile layer (usually  $\sim 100$ – $140$  km).  
 231 Therefore, we use these parameters as a proxy for the lateral extent of metasomatic fluid  
 232 percolation in the lithospheric column, or in other words, for the intensity of metasoma-  
 233 tism at the corresponding depth.

### 234 3.2 Magnetotelluric data and modelling

235 The MT data used in this study were collected as a tremendous collective effort  
 236 by the SAMTEX team. Over a decade-long project, the broad-band and long-period sta-  
 237 tions were set to record at roughly 20-km intervals to investigate the lithospheric archi-  
 238 tecture of the southern African mantle (A. G. Jones et al., 2009). 3D modelling was not  
 239 a practical computational possibility at the time of data collection, so the stations are  
 240 collected in 2D profiles. Most of the data have been published in other studies, utilis-  
 241 ing some parts of the whole dataset (e.g., Evans et al., 2011; Moorkamp et al., 2019; Khoza  
 242 et al., 2013a, 2013b; Muller et al., 2009; Miensofust et al., 2011).

243 The model presented here is produced using the *ModEM* algorithm (Kelbert et al.,  
 244 2014) for the sparsely selected, good-quality data. The model is designed with 15-km-  
 245 sized cells at the core of the mesh. Outside the core zone, 8 cells were inserted, increas-  
 246 ing in length by a factor of 1.5 to reduce the effects of regularisation. The model consi-  
 247 sts of 53 cells in the vertical direction. At the shallowest levels, three 50m-thick cells  
 248 were input to reduce the effects of noise caused by near-surface heterogeneity. Beneath  
 249 this, 50 cells were inserted starting from a 150m-thick layer with an increasing thickness  
 250 factor of 1.15. The ocean was added to the model as a fixed resistivity of  $0.3 \Omega m$ , with  
 251 bathymetry from the ETOPO1 global model (Amante & Eakins, 2009). Twenty-five peri-  
 252 ods between 1-15000 s were chosen for inversion for the sparsely selected, good-quality  
 253 data. Error floors were chosen as 5% of  $\sqrt{Z_{xy}Z_{yx}}$  for all impedance elements.

254 In the first part of this two-part study (Moorkamp et al., 2021), we explored the  
 255 effects of MT modelling imposed by data selection, regularisation methods, initial model  
 256 selection and preference of different modelling algorithms: *ModEM* (Kelbert et al., 2014)  
 257 and *jif3D* (Moorkamp et al., 2011). Results of this study demonstrated that modelled  
 258 mantle conductivities could be affected by the regularisation schemes. For instance, *Mo-*  
 259 *dEM* tends to converge towards the initial model, whereas the *jif3D* model remains rela-  
 260 tively constant as the data sensitivity becomes poorer. To reduce the effects of the regu-  
 261 larisation towards the initial model, we chose to apply a more representative initial model  
 262 in this study. Therefore, the *ModEM* inversion was run from a starting model defined  
 263 using a long-period median-resistivity filter, which allowed smoothly-varying initial model  
 264 resistivities across the model. We constructed this initial resistivity model by: (1) Cal-  
 265 culating the median determinant resistivity values at periods  $> 100$  s for all stations within  
 266 4-degree radius circles centered on each station, (2) assigning that median resistivity value  
 267 to the station at the center of the circle, (3) making linear interpolations between these  
 268 values at each station. Outside the interpolation area,  $\sim 250 \Omega m$  values were used as the  
 269 median value of all stations at periods  $> 100$  s. The inversion run from this median re-  
 270 sistivity half-space had a lower RMS misfit (2.11) than that run from a homogeneous half-  
 271 space (2.17).

272 Compositional interpretation of mantle conductivity requires sensitivity tests to  
 273 be carried out to estimate absolute resistivity values from MT models. We did this by  
 274 selecting the areas of interest for calculating water contents and other compositional pa-

rameters, replacing the modelled resistivities in these areas with blocks of different resistivity values, and testing the impact on data misfit (Figure S1-S5).

### 3.3 Methods for determining the links between garnet xenocryst and MT data

Electrical conductivity can be used to infer the composition of the mantle (e.g., Karato & Wang, 2012; Selway et al., 2019). Compositional interpretation can be achieved by integrating experimental conductivity and petrology studies, thermal structure and phase-mixing models (Özaydın & Selway, 2020). Primarily, the electrical conductivity of mantle minerals depends on temperature through semi-conduction processes. Some additional materials such as structurally-bound hydrogen (expressed below as water) can change the thermal energy required to enhance conductivity (e.g., Wang et al., 2006; Dai & Karato, 2014). The extent to which water can be incorporated into mantle minerals is limited (e.g., Férot & Bolfan-Casanova, 2012; Padrón-Navarta & Hermann, 2017) and in some cases the measured mantle conductivities may require an additional conductive phase, either a mineral with a higher activation enthalpy (e.g., phlogopite) or a very conductive mineral with low temperature dependence (e.g., graphite, sulphides Watson et al., 2010; Zhang & Yoshino, 2017).

We used the program MATE (Özaydın & Selway, 2020) to investigate such relationships. For the water calculations, we used the olivine water-partitioning coefficients of Demouchy et al. (2017) and Novella et al. (2014) for pyroxenes and garnet, respectively. We chose to seek solutions of water content up to limits determined by the olivine solubility model of Padrón-Navarta & Hermann (2017) since it reflects the near-pure  $H_2O$  state of the cratonic mantle in subsolidus conditions. Water contents were modified for both water-solubility and electrical conductivity models to reflect the calibrations of Withers et al. (2012) for olivine and Bell et al. (1995) for pyroxenes and garnet. Our figures show the water content results using three different olivine conductivity models (Dai & Karato, 2014; Wang et al., 2006; Gardés et al., 2014). Different selections of pyroxene and garnet electrical conductivity models do not make considerable differences (Özaydın et al., 2021). We chose to use the conductivity models of Zhang et al. (2012), Liu et al. (2019), Dai & Karato (2009b) and (Y. Li et al., 2017) for orthopyroxene, clinopyroxene, garnet and phlogopite, respectively. For the mixing model, we used the Modified Archie’s model (Glover, 2010). Olivine was set to be a perfectly connected matrix ( $m \ll 1$ ), while interconnectivity of orthopyroxene was set to  $m = 2.5$ . Clinopyroxenes and garnet were set to be not connected with a value  $m = 4$ .

A recent study made detailed comparisons of xenolith water measurements and MT-derived water calculations for the Kimberley-Jagersfontein region (Özaydın et al., 2021) and showed that water contents measured from mantle xenoliths broadly match those interpreted from MT models. Since there are no water content measurements made outside this region in southern Africa, in this work we focus on the trends of the modelled water contents (Figure 7) rather than the specific water contents interpreted from the data.

## 4 Results

### 4.1 Lithospheric architecture from magnetotelluric models

MT models produced in this study demonstrate highly variable mantle conductivities across Precambrian terranes with different ages (Figure 3). Archean cratons (Kaapvaal and Zimbabwe cratons) are depicted as complex regions of mostly resistive lithosphere carved by conductive features, reflecting their metasomatic history. In the Kaapvaal Craton (Figure 2a), this is exemplified by the contrast between the conductive mantle beneath the Bushveld Complex and the resistive center of the Kaapvaal Craton ( $C_1$ -

324  $C_2$ , Figure 2a), which appears to have a convex shape very similar to the mantle keels  
 325 modelled (e.g., Afonso et al., 2008) and imaged by seismic tomography (e.g., Fouch et  
 326 al., 2004; A. Li & Burke, 2006; Ortiz et al., 2019). North of the Bushveld Complex, at  
 327 the northern end of the Kaapvaal Craton, the Archean Pietersburg Terrane also appears  
 328 as a deep resistive feature. Still further north, the Archean Limpopo Belt consists of con-  
 329 ductive mantle starting around  $\sim 50$  km depth (LC) and a complex crustal assemblage  
 330 (Khoza et al., 2013b). The distribution of electrical conductivity in the MT models in  
 331 this region generally resembles previous 2D models (Evans et al., 2011) and 3D models  
 332 made in Limpopo Belt (Khoza et al., 2013b), while being modestly different in terms of  
 333 absolute resistivities and small-scale features in the crust.

334 One of the MT profiles ( $Z_1$ - $Z_2$ , Figure 2h) crosses the Archean Zimbabwe Craton  
 335 on its proposed southwestern edge. The same profile previously modelled with 2D meth-  
 336 ods observed a complex crustal assemblage with a thick resistive root beneath the Zim-  
 337 babwe Craton (Miensopust et al., 2011). These results are similar to ours at the man-  
 338 tle scale, while our model does not exhibit the same complexity in the crust due to larger  
 339 mesh sizes and restricted frequency selection. Going towards the north, the Magondi Belt  
 340 is modelled with a moderately conductive lower crust and mantle, bounded to the north  
 341 by the thick resistive mantle of the Mesoproterozoic Ghanzi-Chobe Belt.

342 Due to the Neogene Kalahari sediments that cover its surface, the structure of the  
 343 Archean-Proterozoic Congo Craton is not well known in most places. The craton is a  
 344 well-defined resistive feature in the westernmost profile near the outcropping Kaman-  
 345 jab Inlier ( $K_1$ - $K_2$ , Figure 2b). However, its high resistivity seems to be limited to spe-  
 346 cific sections within the proposed craton boundaries. Further east (Figure 2c), mantle  
 347 resistivities become considerably lower in the vicinity of profile  $B_1$ - $B_2$  and then increase  
 348 to become again more keel-like in the vicinity of profile  $D_1$ - $D_2$  (Figure 2e). A north-south  
 349 striking conductive feature at lower lithospheric mantle depths beneath the central Congo  
 350 Craton is hinted at in this model but is more prominent in inversions run with more of  
 351 the MT stations included (Moorkamp et al., 2021) and is similar to a structure modelled  
 352 in S- and P-wave tomography studies. Those studies also show that the region surround-  
 353 ing the Kamanjab Inlier has the highest velocities; the lowest velocities are in the cen-  
 354 tral craton and more moderate velocities are modelled near the eastern margin of the  
 355 craton (White-Gaynor et al., 2020). These results suggest that the Congo Craton, as it  
 356 is often mapped (Figure 2,3), might be a fragmented tectonic unit and may consist of  
 357 either a complex tectonic arrangements of blocks of different lithospheric thicknesses or  
 358 may contain relics of past magmatism beneath its Neogene cover.

359 The Proterozoic Reheboth Terrane is imaged as a fragmented feature in which the  
 360 central parts ( $K_2$ - $K_3$ , Figure 2b) have a more conductive lower lithosphere ( $> 100$  km),  
 361 while the northern end nearing the Ghanzi-Chobe region and the Southern Gibeon Fields  
 362 is modelled with a resistive lithosphere. Similarly, other Proterozoic regions between the  
 363 Kaapvaal-Zimbabwe-Limpopo Craton and Congo Craton have similar attributes. The  
 364 youngest of the mobile belts, the Damara Belt, is a Pan-African orogenic zone formed  
 365 during the collision of the Kalahari and Congo cratons in the late Neoproterozoic and  
 366 early Cambrian (Goscombe et al., 2017). As imaged by MT models, the Damara Belt  
 367 consists of a complex crustal assemblage (Khoza et al., 2013a) and a prominent lower  
 368 crustal and upper mantle conductor (Figure 2c,e,3). Variations in the mantle conduc-  
 369 tivity of Proterozoic regions suggests that different processes had different effects on the  
 370 compositional evolution of the mantle.

## 371 4.2 Southern African mantle imaged by garnet xenocrysts

372 A selection of the garnet data from the 100-150 km depth slice is depicted in Fig-  
 373 ures 4 and 5. The ages of the kimberlite eruptions (Figure 4a) are taken from multiple  
 374 sources (Supplementary Material, Tables S1 and S2). In situations where the age of the

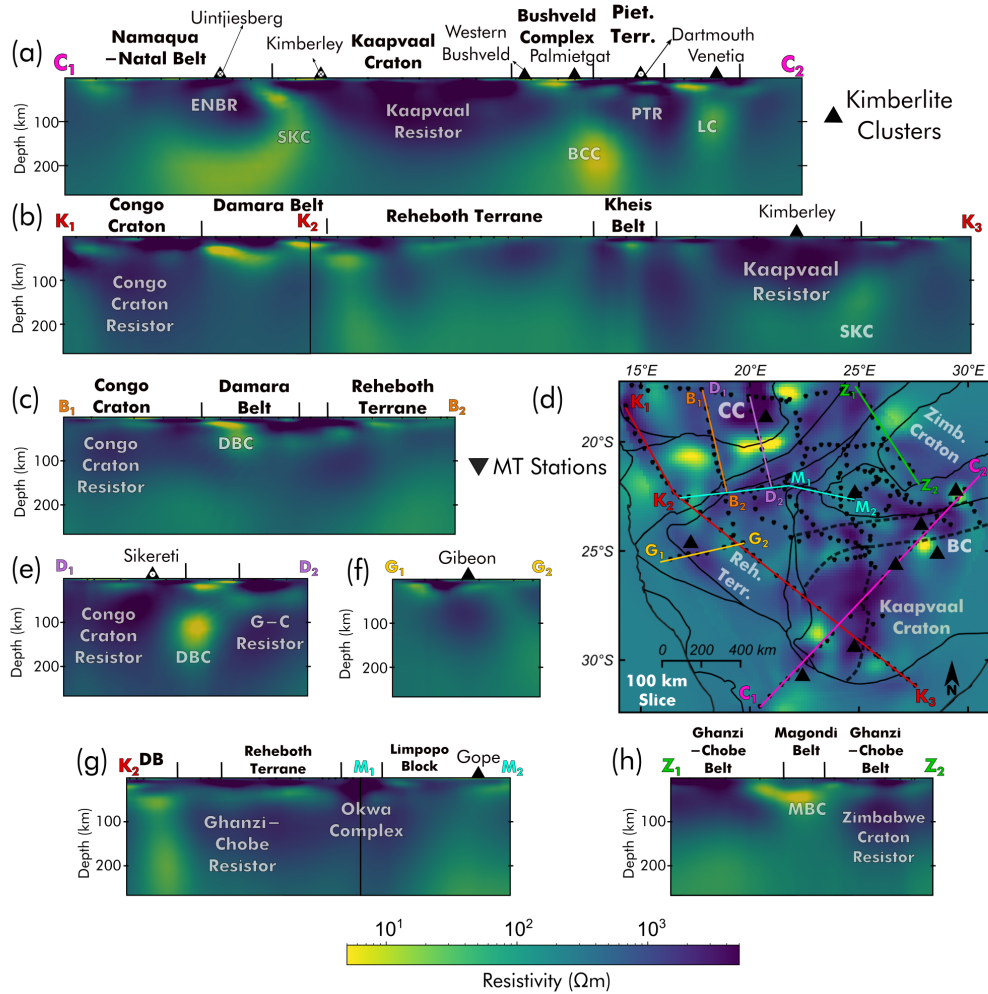


**Figure 2.** Depiction of the 3D MT model of southern Africa in form of vertical cross-sections (a,b,c,f,g,h). Locations of the cross-sections are indicated in (d). BCC: Bushveld Complex Conductor, CC: Congo Craton, DBC: Damara Belt Conductor, ENBR: Eastern Namaqua-Natal Belt Resistor, G-C: Ghanzi-Chobe, LC: Limpopo Conductor, MBC: Magondi Belt Conductor, SKC: Southern Kaapvaal Conductor, PTR: Pietersburg Terrane

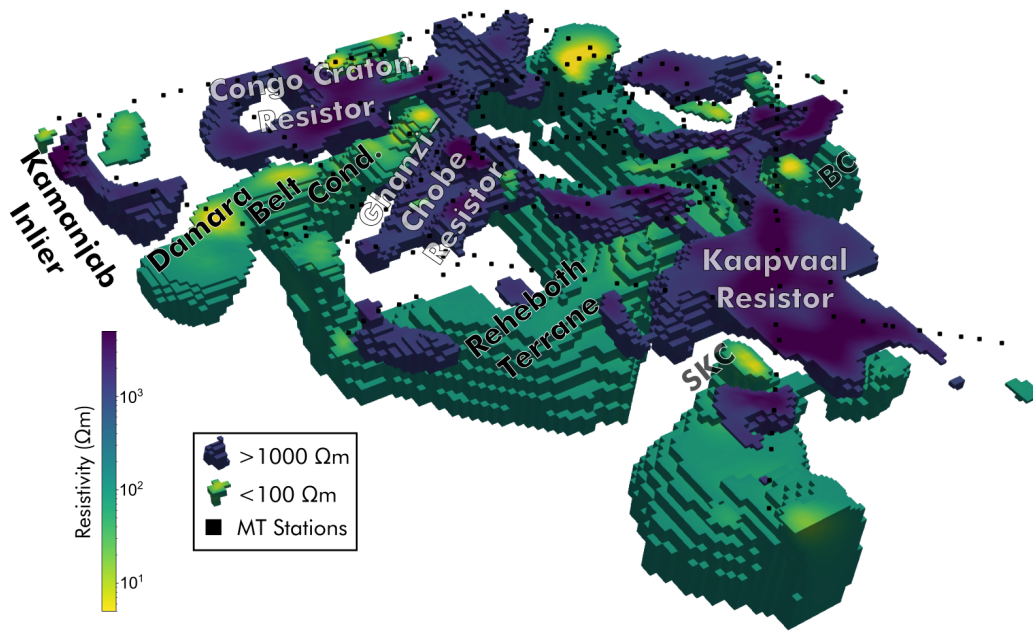


**Figure 3.** 3D contour plot for values  $\leq 1000 \Omega m$  and  $\geq 100 \Omega m$ . BCC: Bushveld Complex Conductor, SKC: Southern Kaapvaal Conductor.

375 pipe was unknown and the geochemical stratification was very similar to the other pipes  
 376 within the same cluster, we assumed the kimberlite to be roughly the same age as that  
 377 cluster. The rest of the unknown ages are represented with black squares. The garnet  
 378 xenocryst analysis illustrates the complexity of the style of metasomatism in southern  
 379 Africa and emphasizes that, from region to region, metasomatic fluids had distinct com-  
 380 positions and/or that the initial formation processes of the mantle rocks differed. For  
 381 instance, iron enrichment (lower  $Mg^{ol}\#$ ) and  $Al_2O_3$  enrichment are not always corre-  
 382 lated even though they can both be regarded as proxies for the fertility of the mantle (Grif-  
 383 fin et al., 2002).

384 Some generalisations can be made from the existing garnet xenocryst database for  
 385 Group I kimberlites:

- 386 1. Lower whole-rock  $Al_2O_3$ , as calculated from Y-in-garnet contents, is a feature of  
 387 a depleted mantle and mostly appears in Archean regions. On the other hand, higher  
 388 values point to either a formerly depleted and then refertilised mantle (e.g., Bushveld  
 389 region) or a mantle that may never have been depleted (e.g., Gibeon).
- 390 2. Similarly, higher  $Mg^{ol}\#$  values signify higher proportions of depleted material,  
 391 while lower values of  $Mg^{ol}\#$  ( $< 92$ ) are more indicative of widespread melt meta-  
 392 somatism. In contrast, higher whole-rock  $Al_2O_3$  values are more likely to be re-  
 393 lated to infiltration of lighter fluids rather than dense and iron-rich melts (Grif-  
 394 fin et al., 2003). Therefore, lower values of  $Mg^{ol}\#$  usually correlate with a shal-  
 395 lower base of the depleted lithosphere, and are more likely to be a feature of the  
 396 thinner Proterozoic terranes with lithospheric thicknesses between 100-150 km (e.g.,  
 397 Okwa and Uintjiesberg clusters, Figure 6).
- 398 3. As expected, the total proportion of metasomatised xenocryst classes is higher in  
 399 non-Archean terranes. One of the main differences between Archean and Protero-

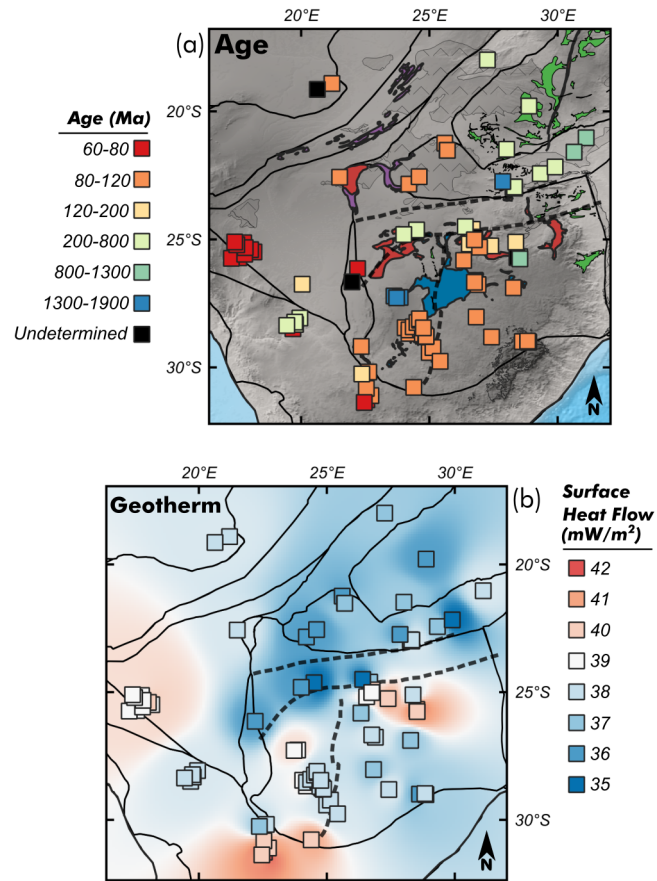


**Figure 4.** (a) Ages of the kimberlites from which garnet xenocrysts are derived. (b) Surface heat flow value corresponding to the generalised cratonic geotherms of Hasterok & Chapman (2011) as derived from the garnet data.

- zoic terranes is the distinct stratification trends observed in Figure 6. Geochemical tomography sections of the Archean mantle usually show a 'depleted layer' between roughly 120-170 km. In contrast, in Proterozoic terranes this depleted material is both less abundant and/or spread throughout the whole depth range in lower proportions.
4. The  $CaO-Cr_2O_3$  classification scheme (Grütter et al., 2004) gives a similar story; Archean units are marked by lower proportions of lherzolitic material compared to their Proterozoic counterparts.
  5. Ti/Zr can be used as a proxy for phlogopite metasomatism whereby medium to low Ti/Zr ratios generally indicate phlogopite-related metasomatism (Griffin et al., 2002). Very high values of Ti/Zr in some Proterozoic areas (Gibeon, Okwa, Sikereti) might indicate that the fertile material at these locations was not affected by phlogopite-related metasomatism. The pipes with high Ti/Zr ratios mostly plot in the fertile fields on Ti-Zr plots. Most of the xenocryst material from which these fields were originally classified came from garnet lherzolites xenoliths in basalts from off-craton areas and are thought to reflect fertile mantle which never experienced a depletion event. The garnets plotted in fertile fields on Ti/Zr plots are typically a feature of younger mantle (Griffin et al., 2002).
  6. 'Unclassified' samples denote garnet analyses that cannot be grouped into the statistically significant types of metasomatism. These garnets most likely reflect the effects of complex metasomatic overprinting, either through multiple episodes by compositionally different fluids. The very high proportions of unclassified garnets observed in the mantle beneath the Bushveld region may indicate such complex metasomatic processes and are associated with a prominent mantle conductor.
  7. Figures 5g and h show the mean chondrite-normalised Nd/Dy and Yb ratios of xenocrysts from the different 'Fertile' classes. Garnets with more sinuous REE and HREE-poor characteristics are more abundant near the core of the Kaapvaal Craton (Kimberley and Kuruman clusters), mirroring the amount of depletion observed. The least sinuous and HREE-rich areas appear on the edges of the cratons or areas immediately surrounding them (Uintjiesberg, Jwaneng) indicating the metasomatism in these areas was more extensive.

## 5 Discussion

If we assume that the connection between composition and electrical conductivity of the mantle can be adequately established through experimental petrology studies, information from garnet xenocrysts and MT models should be compatible. Therefore, we developed interpretations of the southern African lithospheric mantle considering both the broad lithospheric architecture and case by case evaluations of mantle composition. This improves not only our interpretations of MT models, but also of the three-dimensional composition of the southern African lithosphere and our ability to make such interpretations in regions with poorer xenolith constraints.

### 5.1 Resistivity of Archean, Proterozoic, depleted and metasomatised domains

Electrical conductivity distribution of the Archean terranes varies significantly suggesting that metasomatic events left a compositional mark on the initially depleted lithosphere. Similarly, Proterozoic terranes assembled near the Archean cratons do not show consistent characteristics and architectures that would provide a simple relationship between lithospheric thickness, age and composition from the electrical conductivity distribution. The south-central Rehoboth Terrane, for instance, demonstrates lower resistivities ( $K_2-K_3$ , Figure 2b). In contrast, the Gibeon area, which includes one of the clusters of Cretaceous kimberlitic volcanism, is imaged as a highly resistive region. Similarly,

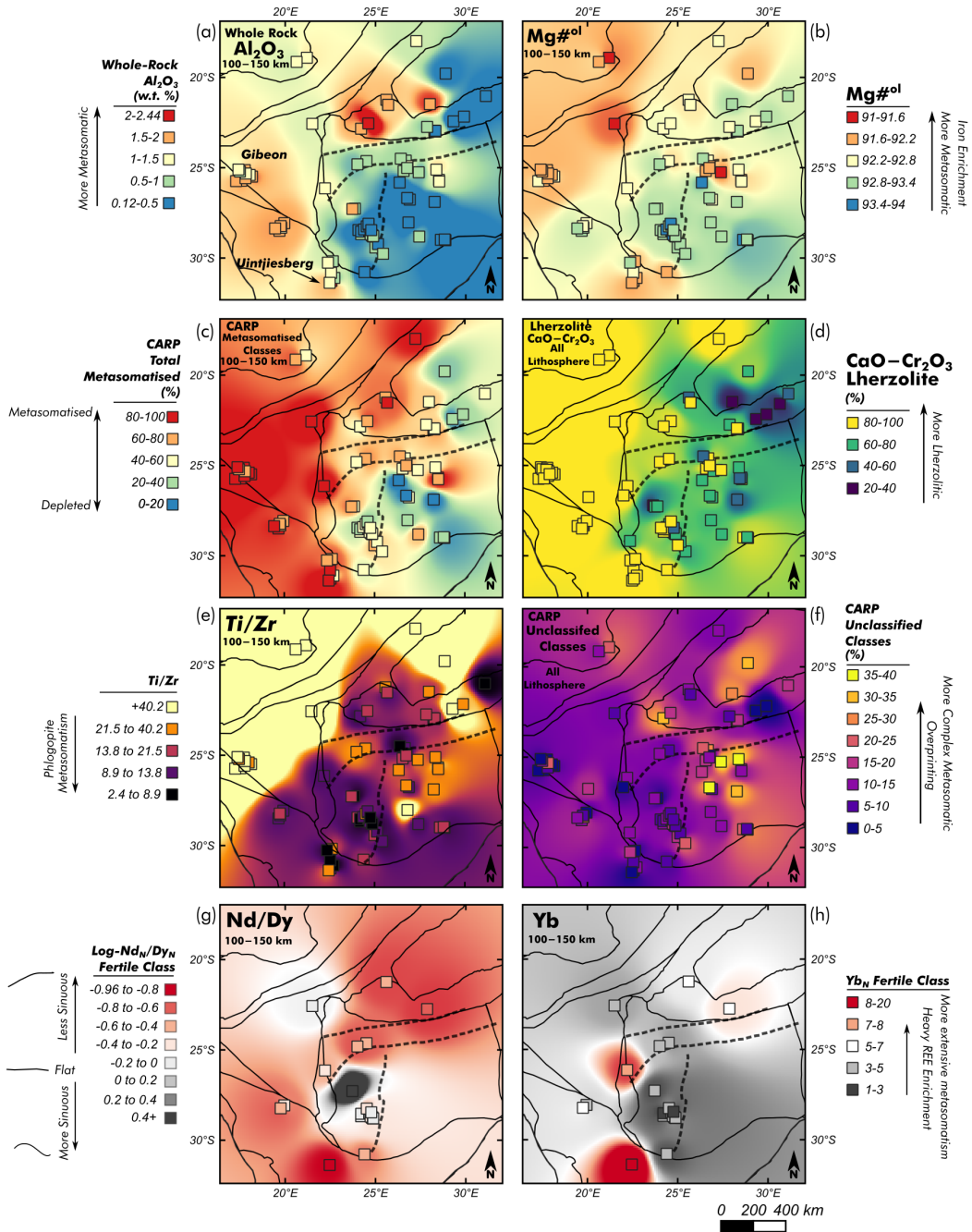


**Figure 5.** Maps of information derived from garnet xenocrysts. Data only exist at kimberlite localities and all other shading is interpolated with a 4-degree inverse distance weighting method. We excluded data points with fewer than 10 samples for the parameter in question. (a) Whole-rock  $Al_2O_3$  contents derived from Y-in-garnet from 100 to 150 km. (b)  $Mg^{ol}\#$  of olivine derived from garnet compositions from 100 to 150 km (c) Total percentage of metasomatic CARP classes: 'Fertile', 'Depleted lherzolite with phlogopite metasomatism' and 'Melt metasomatism'. (d) Percentage of garnets classified as lherzolites from  $CaO - Cr_2O_3$  classification. (e) Ti/Zr ratios of garnets, where lower values indicate phlogopite metasomatism. (f) Percentage of samples that do not fit a defined CARP class, likely to indicate more complex overprinting. (g) Chondrite-normalised log-Nd/Dy taken from garnets classed as 'Fertile'. (h) Chondrite-normalised Yb values taken from garnets classed as 'Fertile'.

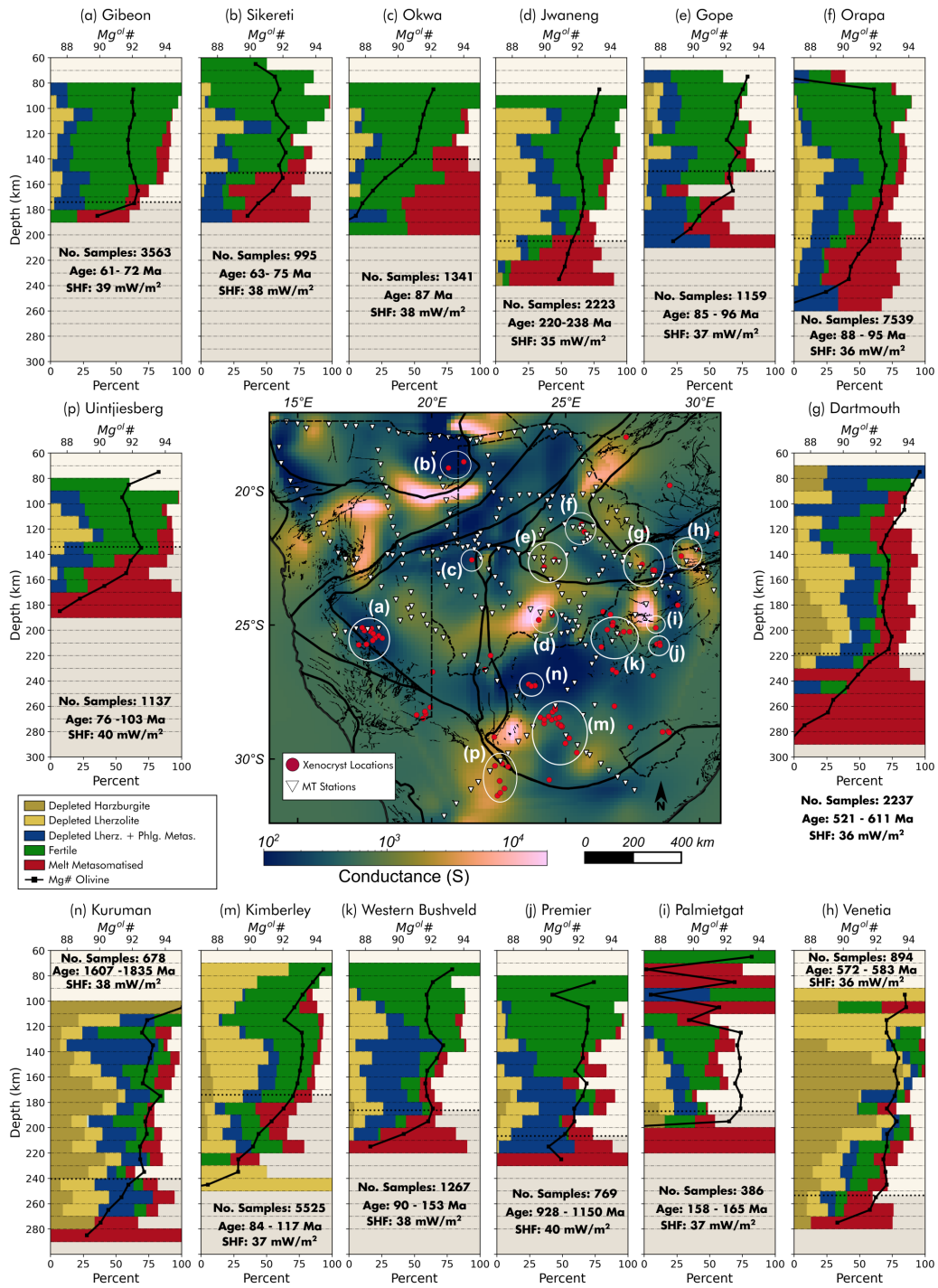


**Figure 6.** Comparison of CARP sections depicted as 10 km interval histograms and olivine  $Mg^{ol}\#$  with modelled mantle conductance (50 - 200 km). Locations of the kimberlite clusters are denoted in the map (a-p). SHF: Surface heat flow value of fitted generalized cratonic geotherm (Hasterok & Chapman, 2011). Horizontal dotted line indicates the base of the depleted lithosphere (BDL).

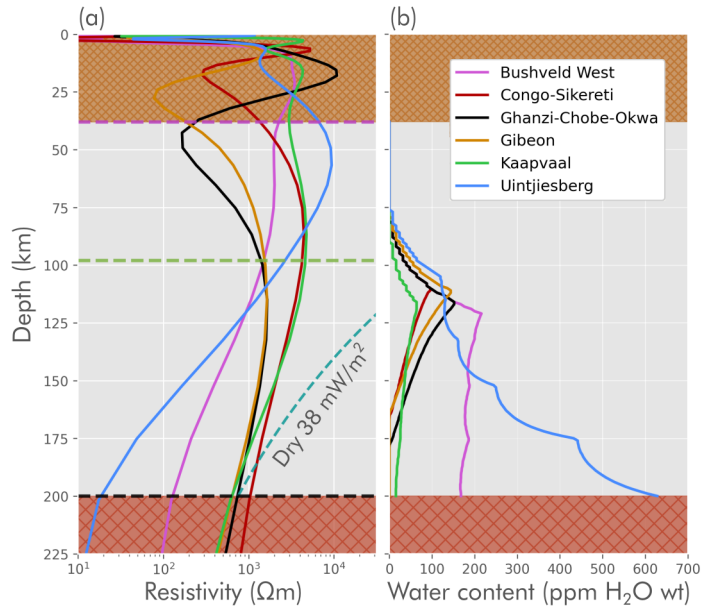


**Figure 7.** (a) Vertical profiles extracted from the 3D model at the locations of: Bushveld West cluster, Congo Craton (Sikereti cluster), Ghanzi-Chobe Belt (Okwa cluster), Gibeon Fields, Kaapvaal Resistor, Uintjiesberg cluster. (b) Water contents calculated from selected areas from the MT model. Bulk rock water contents are calculated up to the distributed olivine water solubility limit defined by the model of Padrón-Navarta & Hermann (2017) for the selected profiles and the thermal structure derived from the nearest kimberlite clusters. Water contents reported in this figure use the calibrations of Withers et al. (2012) for olivine and Bell et al. (1995) for pyroxenes and garnet.

450 the northern end of the Rehoboth Terrane and adjacent Ghanzi-Chobe belt possibly shows  
 451 the greatest depths at which 1000 $\Omega m$  resistivity is observed (Figure 11b). Such high res-  
 452 sistivities have been previously imaged in Proterozoic regions surrounding older cratons  
 453 (e.g., Selway, 2015; Selway et al., 2011) and their high resistivities have been interpreted  
 454 as reflecting magmatic and plate tectonic processes that induced mantle melting and de-  
 455 pletion. In southern Africa, the resistors around the Ghanzi-Chobe Belt line up with the  
 456 1.1 Ga Umkondo magmatic units (Modie, 2000). This area was the focus of rifting and  
 457 extensive melting during the breakup of the Rodinia Supercontinent (De Kock et al., 2014)  
 458 which might have created the depleted resistive mantle with low volatile contents that  
 459 we observe today; similar features are seen in models of the Mozambique Belt, a region  
 460 of Pan-African aged magmatism and high-grade metamorphism and a currently active  
 461 rift zone (Selway, 2015). If the relationship between rifting events and volatile extrac-  
 462 tion from the melting of the mantle can be more confidently linked, the MT models of  
 463 the Ghanzi-Chobe belt may provide evidence for a rifting origin for the Umkondo mag-  
 464 matism (De Kock et al., 2014).

## 465 5.2 Kimberley

466 The Kimberley domain is rich in xenolith-bearing diamondiferous kimberlites from  
 467 which we have 5521 garnet xenocrysts to map the lithospheric mantle. Previous stud-  
 468 ies of garnet xenocrysts have demonstrated that the area was metasomatised by an event  
 469 that occurred between the eruptions of Group II (120-180 Ma) and Group I (90-120 Ma)  
 470 kimberlites (Kobussen et al., 2009; Griffin et al., 2003). Group II kimberlites are pop-

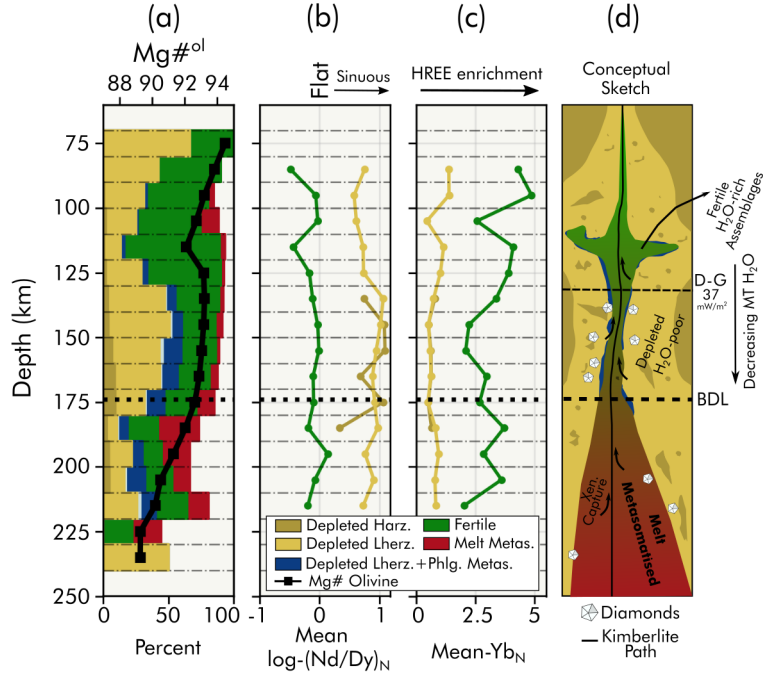


**Figure 8.** Composition of the Kimberley area deduced from garnet xenocrysts depicted as (a) CARP "geochemical tomography" section with  $Mg^{ol}\#$ , (b)  $\log - Nd/Dy_N$  values as a proxy for the sinuosity of garnet REE patterns, (c)  $Yb_N$  values as a proxy for HREE enrichment. (d) Conceptual sketch of the interpreted compositional section considering the water content interpretation of Özaydın et al. (2021). D-G: Diamond Graphite transition at  $37\text{ mW/m}^2$  geotherm, BDL: Base of the depleted lithosphere.

471 ulous in this area, reflecting modal metasomatic modification of the mantle prior to kimberlite emplace-  
 472 ment (Giuliani et al., 2015).

473 The Kimberley-Jagersfontein area is geochemically stratified into three layers: (a)  
 474 A fertile layer between 90-130 km that is marked by lower  $Mg^{ol}\#$  values, (b) a depleted  
 475 layer between 125-175 km and (c) an underlying melt-metasomatised layer. Our MT re-  
 476 sults demonstrate that the Kimberley domain overlies a lithosphere with relatively low  
 477 resistivities (the greatest depth at which  $1000\ \Omega m$  is modelled is  $\sim 100\text{--}120$  km, Fig-  
 478 ure 11b) compared to the main Kaapvaal resistor ( $> 150$  km, Figure 11b). The conduc-  
 479 tive nature of the lithosphere beneath 100 km might reflect the chemical alteration ob-  
 480 served in garnet xenocrysts.

481 In a recent study, Özaydın et al. (2021) compared garnet xenocrysts, xenolith water  
 482 contents and MT models in the Kimberley-Jagersfontein region. These analyses demon-  
 483 strated that water contents calculated from MT models decreased with depth between  
 484 100 to 160 km, which roughly agrees with the measured xenolith water contents. How-  
 485 ever, a larger misfit was observed in the depleted layer, suggesting a local metasomatic  
 486 control around kimberlite conduits. Since the fertile layer corresponds to a water-saturated  
 487 zone and calculated water contents can account for observed xenolith water contents, the  
 488 authors considered the metasomatism in the fertile layer has to be laterally extensive enough  
 489 to be sensed by electromagnetic fields. In support of this argument, we found that  $\log -$   
 490  $Nd/Dy_N$  and  $Yb_N$  values correlate with the number of garnets classified as metasoma-  
 491 tised in the fertile layer (Figure 8). Given that increasing metasomatism leads to less sin-  
 492 uous  $\log - Nd/Dy_N$  patterns and more HREE enrichment in garnet xenocrysts (Griffin

493 et al., 2002), we suggest that the metasomatic fluids pervasively percolated through the  
 494 fertile layer, peaking around 110-120 km depth. As a result, the kimberlites sampled more  
 495 fertile material at this depth.

496 A conductor bounds the Kimberley region to the east (Figure 2a). Like the Molopo  
 497 Farms and the Bushveld complexes, this conductor coincides with a large Paleoprotero-  
 498 zoic mafic intrusive complex (1.9 Ga, Maier et al., 2003), the Trompsburg Complex (TC,  
 499 Figure 1). Since it does not have surface exposure, existing knowledge about the com-  
 500 plex is limited to gravitational modelling and few borehole measurements (Rezaie et al.,  
 501 2017). We think the conductor here may be related to the emplacement of the mafic mag-  
 502 mas and a metasomatised residue.

### 503 **5.3 Bushveld magmatic event and its effects on composition of the litho-** 504 **sphere**

505 The Bushveld Complex (BC) is a large igneous body emplaced between 2.055-2.06  
 506 Ga, intruding Transvaal Group sediments (Scoates et al., 2021). The complex outcrops  
 507 as mafic-ultramafic eastern, western and northern lobes (Rustenberg Layered Suite) and  
 508 slightly younger felsic rocks towards the centre (Figure 9a). A strong stratigraphic and  
 509 geochemical concordance between the mafic intrusives in the different lobes suggests con-  
 510 nectivity between them or a co-genetic relationship (Kruger, 2005). Gravity models of  
 511 the Bushveld Complex demonstrate that surface exposures of the complex are contin-  
 512 uous at depth and define a lopolith structure with a maximum thickness exceeding 8 km  
 513 (Cole et al., 2014). The Palmietgat kimberlite pipe, near the centre of the Bushveld Com-  
 514 plex, contains xenoliths of plagioclase-bearing lower-crustal pyroxenites petrologically  
 515 akin to the pyroxenites of the Rustenberg Layered Suite, indicating connectivity between  
 516 the underlying western and eastern lobes (Webb et al., 2011). Zircon U-Pb dating con-  
 517 strains the emplacement of the Rustenberg Layered Suite to a one million year time win-  
 518 dow, indicating extremely high magma fluxes (Zeh et al., 2015). The lower units of the  
 519 Rustenberg Layered Suite hold economically valuable, PGE-hosting chromitite layers (e.g.,  
 520 Merensky Reef) that contain more than 80% of global platinum reserves (VanTongeren,  
 521 2017). Both the source of the parental magma and the magma chamber differentiation  
 522 processes necessary to produce such PGE-rich chromitite layers are still debated (Cawthorn,  
 523 2015; VanTongeren, 2017). Considering the targeting depths of our MT models, the most  
 524 relevant ideas to investigate are speculations about the mantle component required in  
 525 the parental magmas to generate the specific properties observed in the intrusives (Zi-  
 526 rakparvar et al., 2014; Richardson & Shirey, 2008).

527 More than ten adjacent magmatic bodies, each with geochemical affinities to the  
 528 BC, were emplaced during the same narrow time window (Figure 9a, Rajesh et al., 2013),  
 529 and generally are considered to be satellite intrusions. One of these satellite magmatic  
 530 bodies, the Molopo Farms Complex (MFC, Figure 1), is a layered mafic intrusion sit-  
 531 uated in southern Botswana roughly 400 km west of BC (Beukes et al., 2019). The strati-  
 532 graphic layering of the MFC is similar to the lower layers of the BC, but available bore-  
 533 hole data indicate it lacks the PGE-rich chromitite layers (e.g., Kaavera et al., 2018). The  
 534 BC and these satellite intrusions may have formed as part of a larger Bushveld Large  
 535 Igneous Province, which used a structural weakness corridor along the Thabazimbi-Murchison  
 536 Lineament (TML, Rajesh et al., 2013).

#### 537 **5.3.1 Garnet xenocrysts and composition of the Bushveld mantle**

538 Garnet xenocrysts that sampled the mantle in the vicinity of the BC show more  
 539 variable geochemical signatures from pipe to pipe, in contrast to those from Proterozoic  
 540 terranes or those from the Kimberley region. They are concentrated around the BC or  
 541 close to the limbs of the Rustenberg Layered Suite. Only the Palmietfontein and Palmi-  
 542 etgat pipes fall within the boundaries of the complex. Compared to those from the south-

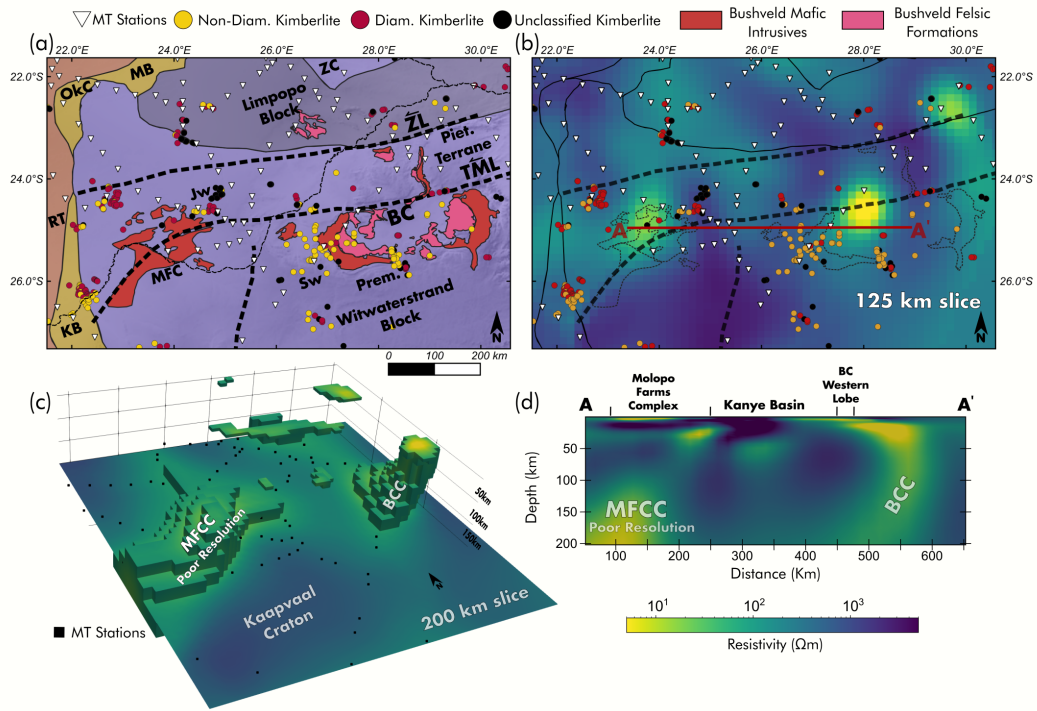


**Figure 9.** (a) Map of the region containing Bushveld-aged formations with diamondiferous (diam., red) and non-diamondiferous (non-diam., yellow) kimberlites. (b) MT model at 125 km depth of the same region. (c) A - A' vertical section from the MT model. A - A' is indicated in (b). (d) Contour plot of the MT model. The 3D contour surface encloses regions with resistivities less than 100  $\Omega m$ . BC: Bushveld Complex, BCC: Bushveld Complex Conductor, Jw: Jwaneng Region, MFC: Molopo Farms Complex, MFCC: Molopo Farms Complex Conductor, MB: Magondi Belt, OkC: Okwa Complex, Prem: Premier Region, Sw: Swartruggens Region, RT: Rehoboth Terrain, KB: Kheis Belt, ZC: Zimbabwe Craton.

543 western pipes, the garnet xenocrysts from the pipes near the BC demonstrate higher whole-  
 544 rock  $Al_2O_3$ , lower  $Mg^{ol}\#$ , a general increase in metasomatic classes and a lack of de-  
 545 pleted material (Figure 5c,d,e).

546 The Palmietgat pipe is one of the very few kimberlite pipes emplaced near the centre  
 547 of the BC (Figure 6i). Quite a high proportion of the garnets here (41%) do not fall  
 548 into statistically significant CARP classifications associated with a consistent metaso-  
 549 matic signature. The high proportion of unclassified garnets at the Palmietgat pipe may  
 550 indicate complex metasomatic overprinting, with multiple episodes of melts and fluids  
 551 using the same conduits. A general increase in the proportion of unclassified samples near  
 552 the BC can be seen in Figure 5f, suggesting the metasomatic signature in the area is highly  
 553 complex.

554 The kimberlite cluster immediately west of or penetrating the western limb of the  
 555 Bushveld Complex (Western Bushveld, Figure 6i) exhibits a thick layer of depleted lher-  
 556 zolites with phlogopite metasomatism between 130-160 km. Like other sections near the  
 557 Bushveld Complex, many unclassified samples come from this middle section (130-170 km).  
 558 These unclassified samples fall into wehrlite and low-Cr  $CaO - Cr_2O_3$  classifications  
 559 at the fertile layer and beneath the BDL, whereas they appear to be lherzolitic in the  
 560 middle section. The Palmietfontein pipe (Figure S21c), like the Premier sections (Fig-  
 561 ure S22c), completely lacks samples from this middle section where the unclassified gar-  
 562 nets are most populous.

563 Just south of the BC, the Premier kimberlite cluster (Figure 6j) is considerably older  
 564 (928-1150 Ma) and yields higher equilibration temperatures ( $40mW/m^2$ ) compared to  
 565 the Bushveld West cluster and the Palmietgat pipe (90-153 Ma,  $38mW/m^2$ ). The amount  
 566 of secular cooling expected between 928 Ma and 153 Ma is around ( $82C^\circ$ , Shu et al., 2014),  
 567 a value similar to the difference in geotherms between the two clusters ( $\sim 50-100C^\circ$ ).  
 568 Therefore, the area is not likely to have been impacted by a large thermal event between  
 569 these times. This is consistent with the similarity of the geochemical 'tomography' sec-  
 570 tions showing a large portion of unclassified samples and depleted lherzolites with phl-  
 571 ogopite metasomatism in the middle of the section. Like the Palmietfontein pipe of the  
 572 Bushveld West cluster, the Premier and Franspoort pipes have entrained a relatively low  
 573 number of garnets from this middle section (Figure S10c, S22c); it is probable that the  
 574 strong metasomatism has destroyed most pre-existing garnet in the rocks at these lev-  
 575 els.

576 The mantle beneath the Molopo Farms Complex (MFC), on the other hand, is sam-  
 577 pled most closely by the Triassic-aged Jwaneng and Thankane kimberlite pipes (Figure  
 578 6d). The equilibration temperatures of the sampled xenocrysts are lower than in the BC  
 579 ( $35$  vs.  $38 mW/m^2$ ). The lower geotherm might indicate that the event that increased  
 580 the geotherm beneath the Bushveld Complex, whether it be the main Bushveld event  
 581 or not, did not affect the mantle near MFC at a similar scale. Geochemical stratifica-  
 582 tion in these pipes is also more akin to the mantle beneath the Kimberley domain, where  
 583 an increased population of depleted material is evident at mid-lithosphere depths.  $REE_N$   
 584 patterns display trends of metasomatic intensity at depths similar to those observed in  
 585 Kimberley. A peak metasomatic intensity (lowest  $\log-Nd_N$   $Dy_N$ , highest  $Yb_N$ ) is ob-  
 586 served at 125 km (Figure S43). However, base-level rates of  $\log-Nd_N$   $Dy_N$  are much lower  
 587 than the Kimberley (Figure 5g), suggesting metasomatic effects might be more exten-  
 588 sive or that the area originally underwent less depletion.

### 589 **5.3.2 Bushveld geoelectric structure and other geophysical studies**

590 In our MT models, the Bushveld region shows marked lateral heterogeneity with  
 591 some strongly conductive vertical sections extending towards the crust (e.g., BCC, Fig-  
 592 ure 9). The Thabazimbi-Murchison Lineament (TML) crosses three contrasting man-  
 593 tle electrical domains: a conductive lower lithospheric mantle and resistive upper litho-

spheric mantle in the vicinity of the Molopo Farms Complex, a resistive keel-like area beneath the Kanye Basin and a very conductive lithospheric mantle associated with the BC (Figure 9a). Broadly, such resistivity differences can either have thermal or compositional causes. S-wave seismic receiver function studies give no clear indication of a thinned mantle lithosphere beneath this region (Ravenna et al., 2018; Sodoudi et al., 2013). However, the Bushveld region is associated with lower S and P wave velocities (e.g., Ortiz et al., 2019; Youssof et al., 2013; Fouch et al., 2004) which suggests a chemical/metasomatic origin of the conductive anomalies rather than a thermal one (Griffin et al., 2009).

Seismic receiver function analyses indicate that the western-central area of the BC is marked by a relatively high crustal thickness ( $\sim 49$  km) with a more gradual Moho transition compared to sharper waveforms observed in the surrounding crust (Youssof et al., 2013; Delph & Porter, 2015). Kgaswane et al. (2012) also suggest structural complexity at crustal depths to account for observed receiver functions. The depressed Moho can be a sign of underplating by mafic intrusions (O'Reilly & Griffin, 2013). This anomalous zone overlies the Bushveld mantle conductor (BCC), extending from  $> 200$  km to near-surface where the MT transect crosses the TML. This region is a good candidate for a zone of mechanical weakness in the lithosphere where the Bushveld magmas could ascend and precipitate interconnected conductive minerals. The TML has been invoked many times before as the feeder location for the Bushveld magmatic units (e.g., Clarke et al., 2009). Such Moho complexity and localized increased Moho depths are not observed beneath the Molopo Farms Complex, which instead overlies gradual decreases in both Moho complexity and crustal thickness (Delph & Porter, 2015; Youssof et al., 2013).

The mantle beneath the Molopo Farms Complex has been modelled to be conductive at depths greater than  $\sim 110$  km but the resolution of this conductor is not robust and this feature is not as strong in the other inversion models (Moorkamp et al., 2021). At shallower depths, resistivities are comparable to the mantle beneath the Kanye Basin. If we assume similar parental magmas for the BC and MFC, the differences in resistivity of the mantle beneath them may suggest: (1) The magma emplacement that caused the MFC was not as focused as that which caused the BC, or the volume of magma intruding the lithosphere was smaller, (2) the MFC was not emplaced from deep feeder dykes but instead magmas flowed horizontally from the primary Bushveld magma source, most likely along the TML (Prendergast, 2012). Our models can not differentiate between these emplacement models but provide evidence for conductive metasomatic signatures beneath. However, if one expects similar mantle compositional sections from the BC and the MFC and a geotherm indicating lack of thermal impact beneath the MFC, the second option may seem more probable. A denser MT data collection around both areas may help to address this situation.

### 5.3.3 *Compositional causes of conductivities*

We have tested different compositional scenarios to fit the observed ranges of conductivity of the mantle beneath the Bushveld region. The thermal structure was constrained using the  $38 \text{ mW/m}^2$  geotherm derived from garnet xenocryst data for the Cretaceous Group I kimberlites around the western lobe of the Bushveld Complex (Figure 6k) and the Jwaneng-Thankane pipes ( $35 \text{ mW/m}^2$ ). The Bushveld geotherm agrees well with other calculations derived from measured heat flow and crustal heat generation data (M. Jones, 2017). Similarly, thermobarometry data calculated with the method of Nimis & Taylor (2000) from Jwaneng samples fits a geotherm of  $36.3 \text{ mW/m}^2$  (Figure S62, Preston & Sweeney, 2003). These results imply that with the maximum water contents allowed by the water solubility model (Padrón-Navarta & Hermann, 2017) and water-partitioning coefficients (Figure 10a, Demouchy et al., 2017), the water in NAMs in a lherzolitic mantle cannot explain the conductivities observed.

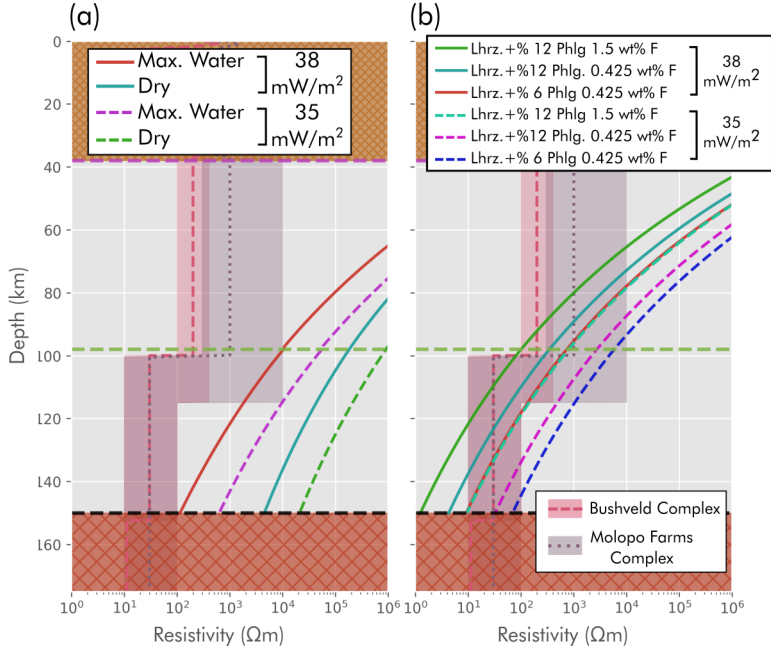


**Figure 10.** Comparisons between resistivities from the Bushveld and Molopo Farms complexes and theoretical calculations of electrical conductivity. (a) Bushveld Complex (red) and Molopo Farms (magenta) resistivities with resistivity depth curves calculated at hydration saturation determined using the olivine solubility model of Padrón-Navarta & Hermann (2017) and water-partitioning coefficients from Demouchy et al. (2017) and Novella et al. (2014) for pyroxenes and garnet, respectively. (b) Resistivity-depth curves calculated for a lherzolite composition with varying amounts of perfectly connected phlogopite. The electrical conductivity models used for the models are as follows: Olivine: Dai & Karato (2014), Orthopyroxene: Dai & Karato (2009a), Clinopyroxene: Liu et al. (2019), Garnet: Dai & Karato (2009b), Phlogopite: Y. Li et al. (2017).

644 Another possible explanation for such conductive mantle is the existence of well-  
 645 connected fluorine-bearing phlogopite (Y. Li et al., 2017). Abundant phlogopite-style meta-  
 646 somatism is observed in almost all compositional sections near the Bushveld region (Fig-  
 647 ure 6). However, these signatures do not necessarily indicate the presence of perfectly  
 648 connected phlogopite grains since they are the byproducts of reactions in which phlo-  
 649 gopite replaces sparsely distributed garnets (Van Achterbergh et al., 2001). However, phl-  
 650 ogopite could still precipitate on boundaries between NAM grains during percolation of  
 651 metasomatic fluid or melt. Such a model with conductive phlogopites can also be envi-  
 652 sioned as peridotites veined with MARID (Mica-Amphibole-Rutile-Ilmenite-Diopside)  
 653 and PIC (Phlogopite-Ilmenite-Clinopyroxene) assemblages (Foley, 1992). This model of  
 654 hydrous mineral emplacement is more likely to produce a mantle with highly intercon-  
 655 nected phlogopite. We used the median F (fluorine) contents of glimmerite (MARID)  
 656 xenoliths ( $\sim 0.425$  w.t.) as a realistic estimate and the maximum F content of all peri-  
 657 dotite mantle xenoliths ( $\sim 1.5$  w.t.) as a bound on maximum conductivity that can be  
 658 observed (Figure S61). For modal compositions, we derive a lherzolitic matrix with 12%  
 659 and 6% of perfectly interconnected phlogopite. With these compositions, the conduc-  
 660 tivity of the mantle beneath Bushveld Complex can be explained below 100-120 km with  
 661 6% and 12 % phlogopite with 1.5 wt% and 0.425 wt% F, respectively. The same com-  
 662 positions would explain conductivities at relatively greater depths ( $\sim 120 - 150$  km)  
 663 in the colder mantle ( $35 \text{ mW/m}^2$ ) beneath the Molopo Farms Complex.

664 It is impossible to model the conductor beneath the Bushveld Complex above 110 km  
 665 (BCC) using experimental electrical conductivity data for the major rock-forming min-  
 666 erals existing in the mantle (olivine, pyroxenes, garnet, phlogopite and amphibole; Fig-  
 667 ure 10). Therefore, the conductivity requires minor accessory minerals such as graphite  
 668 or sulphides, either as films on the edges of grains or as crystalline material precipitated  
 669 from a metasomatic fluid (Pearson et al., 1994). However, the behaviour of these ma-  
 670 terials in a peridotitic matrix is not well understood, and some existing studies are in  
 671 apparent conflict with each other (Wang et al., 2013; Zhang & Yoshino, 2017). Graphite,  
 672 for instance, may establish an effective conductivity with higher than usual amounts of  
 673 carbon in the mantle ( $> 1.6\%$  vol., Wang et al., 2013). However, other authors suggest  
 674 that graphite films are not stable with more realistic concentrations of carbon in the sam-  
 675 ple ( $\ll 0.8\%$  Zhang & Yoshino, 2017; Watson et al., 2010) and the previous results of  
 676 Wang et al. (2013) may have only been the result of temporally limited crystallisation,  
 677 which would not retain its interconnection given enough time (Zhang & Yoshino, 2017).  
 678 Furthermore, the nature of carbon speciation in the mantle is not well understood, and  
 679 the processes that bring xenoliths to the surface may result in compositionally biased  
 680 xenolith samples (Stagno et al., 2019). For instance, some rare xenoliths from the Pre-  
 681 mier and Jagersfontein kimberlites are very rich in large veins of crystalline graphite (Pear-  
 682 son et al., 1994), suggesting that crystalline graphite might be underrepresented in xeno-  
 683 liths since they are likely to be destroyed by the carrier magma. On the other hand, the  
 684 Palmietgat kimberlite is diamondiferous (Webb et al., 2011), which suggests the possi-  
 685 ble existence of graphite above the graphite-diamond transition.

686 Recent detailed studies on peridotite mixtures with magnetite (Dai et al., 2019)  
 687 and chromite (W. Sun et al., 2021) showed that these types of minor constituents might  
 688 have very different percolation thresholds before they dominate electrical conduction in  
 689 an assemblage, probably reflecting their precipitation behaviour in the matrix. The per-  
 690 colation threshold represents the volume needed for a mineral to dominate the electri-  
 691 cal conduction in an assemblage. While it is hard to reconcile any of the required vol-  
 692 umetric abundances used in these experiments to reflect the actual state of the mantle  
 693 (16% for chromite, 1.5% for magnetite), they illustrate the possibility that such phases  
 694 could have a significant effect on metasomatised portions of the mantle.

695 Nevertheless, all Bushveld aged magmatism in the Kaapvaal Craton is strongly as-  
 696 sociated with a conductive signature in the MT models, which supports the idea that

697 the generation and emplacement of Bushveld magmas left a metasomatised signature in  
 698 the lithospheric mantle (e.g., Zeh et al., 2015; Richardson & Shirey, 2008).

#### 699 **5.4 Namaqua-Natal Belt and Uintjiesberg**

700 Southwest of the Kimberley area and over the proposed craton boundary, a differ-  
 701 ent geoelectrical structure is apparent. Here, MT models indicate a lithosphere composed  
 702 of a body (Eastern Namaqua-Belt Resistor, ENBR) that is highly resistive above 100-  
 703 120 km and much less resistive below that depth (Figure 2a). Due to the thick Karoo  
 704 sedimentary sequence, it is not entirely clear whether the southern limit of this resistive  
 705 area is the border of the Kaapvaal Craton or not (Weckmann, 2012; Kobussen et al., 2008).  
 706 However, the continuation of potential field lineaments alongside the Kheis Belt units  
 707 suggests that the existing craton boundary coincides with our so-called suture zone (Cor-  
 708 ner & Durrheim, 2018). The significantly deeper Moho depths south of this boundary  
 709 (Youssof et al., 2013; Delph & Porter, 2015) and the Proterozoic ages of the lower crustal  
 710 granulite xenoliths from kimberlite clusters (Schmitz & Bowring, 2004) also suggests that  
 711 the existing craton boundary runs through this location. We suggest that this resistor  
 712 represents a Paleoproterozoic microcontinental block at the northernmost front of the  
 713 Namaqua-Natal Belt where it collided with the Kaapvaal Craton.

714 Around the eastern Namaqua-Belt Resistor, the Uintjiesberg cluster consists of non-  
 715 or weakly-diamondiferous Group I kimberlites (76-103 Ma, Figure 4a). Garnet xenocrysts  
 716 indicate a mantle section with higher equilibration temperatures ( $40 \text{ mW/m}^2$ ) than the  
 717 nearby Kimberley region ( $37 \text{ mW/m}^2$ ). The Group I thermal structure (Figure 4b), geo-  
 718 electric architecture (Figure 2a) and calculated water contents (Figure 7) are consistent  
 719 with a shallower base of the depleted lithosphere (135 km, Figure S40) and a higher pro-  
 720 portion of melt-metasomatised classes, suggesting the region experienced extensive meta-  
 721 somatism during a thermal event (Kobussen et al., 2008). Differences in temperature and  
 722 chemistry between Group I and Group II kimberlites in the region also suggest that ex-  
 723 tensive melt-infiltration and metasomatism occurred between these times, raising the base  
 724 of the depleted lithosphere by  $\sim 40$  km (Kobussen et al., 2008).

725 From just above the base of the depleted lithosphere, a sudden drop in mean Ti/Zr  
 726 ratios is evident and continues up to 110 km, suggesting phlogopite-related metasoma-  
 727 tism at these depths. Considering that this layer (110-140 km) coincides with a layer of  
 728 low resistivity in the MT models, it might be rich in interconnected phlogopites. How-  
 729 ever, electrical conductivity calculated with a perfectly connected phlogopite of 5-10 %  
 730 with 0.425 wt% F is roughly an order of magnitude more conductive than modelled res-  
 731 istivities (Figure S6). This calculation indicates that electrical conductivities observed  
 732 in the region are likely due to water in NAMs and not due to minor interconnected phl-  
 733 ogopite. Fertile garnets in Uintjiesberg cluster also demonstrate the least sinuous pat-  
 734 terns with strong HREE enrichment (Figure 5g,h). However, most of these garnets are  
 735 between 100 and 110 km depth, where lower Ti/Zr values are not observed, suggesting  
 736 that the metasomatic signature might not be as extensive at these depths.

#### 737 **5.5 Limpopo Belt**

738 The Limpopo Belt is a continental block wedged between the Zimbabwe and Kaap-  
 739 vaal cratonic assemblages. Seismic tomography models demonstrate the existence of a  
 740 thick cratonic lithosphere with fast velocities beneath the Limpopo Belt (Fouch et al.,  
 741 2004; A. Li & Burke, 2006; Ortiz et al., 2019; Youssof et al., 2015). However, these mod-  
 742 els also show a seemingly fragmented structure, with relatively slower velocities in the  
 743 eastern Limpopo Belt. These slower velocities may be attributed to metasomatism re-  
 744 lated to intense and pervasive Jurassic Karoo magmatism. Many authors have envisioned  
 745 that the Karoo plume head was centred roughly on the eastern Limpopo Belt, based on  
 746 the distribution of dyke swarms and volcanism radiating from the area (Figure 1, KTJ,

747 Jourdan et al., 2006). Whether or not the Karoo event was initiated by a mantle plume  
 748 related to the Gondwana breakup, the eastern Limpopo Belt seems to be the centre of  
 749 intense Jurassic volcanism.

750 Our MT models show that the Eastern Limpopo Belt comprises a highly conduc-  
 751 tive lower crust ( $\leq 10\Omega m$ ) underlain by a highly conductive mantle. Sensitivity tests  
 752 show the mantle between 50 to 100 km depth can be fit by a block with resistivities  $\sim$   
 753 60–100 $\Omega m$ . Like the Bushveld Complex, the region also exhibits locally increased Moho  
 754 depths with gradual velocity gradients (Youssof et al., 2013; Delph & Porter, 2015), which  
 755 may suggest mafic underplating.

756 Garnet xenocrysts from kimberlites in the Venetia cluster, which was emplaced around  
 757 the time of Gondwana assembly ( $\sim 572$ – $583$  Ma), indicate a considerable proportion  
 758 of depleted harzburgites and lherzolites compared to the Kimberley area (Figure 6h).  
 759 The high conductivity (Figure 6,2a) and lower seismic velocities modelled in the area do  
 760 not reflect these garnet xenocryst compositions. The discrepancy between xenocrysts and  
 761 geophysical models point to metasomatism of the lithospheric mantle that post-dated  
 762 eruption of the Venetia kimberlites, likely to be effects of the  $\sim 180$ Ma Karoo event,  
 763 as previously suggested by Griffin et al. (2003).

## 764 5.6 Gibeon Fields

765 The Gibeon region stands out on the MT models with its resistive root and young,  
 766 non-diamondiferous kimberlite cluster (Figure 6,11) around a relatively resistive region.  
 767 The region is roughly situated within the Rehoboth Terrane along the boundary with  
 768 the Namaqua-Natal Belt and is marked by a sudden drop in magnetic intensity (Cor-  
 769 ner & Durrheim, 2018). The kimberlites here are among the youngest in southern Africa  
 770 (60–72 Ma) and are considered to be related to the same plume responsible for the em-  
 771 placement of Group I kimberlites in Kimberley (Davies et al., 2001). Garnet xenocrysts  
 772 shows a mantle section mostly made up of fertile lherzolites with relatively constant  $Mg^{ol}\#$   
 773 (Figure 6a). Unlike what is observed in the Archean regions and the Uintjiesberg clus-  
 774 ter, almost all of the fertile samples have high-Ti and low-Zr signatures likely to indi-  
 775 cate low degrees of phlogopite metasomatism (Figure 5e). The geotherm derived from  
 776 garnet xenocrysts can only be estimated from low temperature garnets while high tem-  
 777 perature estimates seem to be scattered, similar to observations in other thermobarom-  
 778 etric calculations (Bell et al., 2003) and likely to be an effect of melt-metasomatism  
 779 beneath the depleted lithosphere. Two-pyroxene thermobarometry (Brey & Köhler, 1990)  
 780 carried out by Bell et al. (2003) fits best to a conductive 41.5  $mW/m^2$  geotherm if the  
 781 high temperature samples between 4-5 GPa are excluded. While these high temperature  
 782 samples may indicate melt-related metasomatism, there is no indication of large scale  
 783 melt infiltration in the geochemical tomography section and stable ( $Mg^{ol}\# = 92$ ) val-  
 784 ues are observed.

785 Since the 3D MT model shows a highly resistive region with low estimated water  
 786 contents, we propose that the mantle here might not be extensively metasomatised. The  
 787 high resistivities suggest that there is no pervasive phlogopite metasomatism, while the  
 788 abundant fertile lherzolites may indicate that the mantle never really experienced strong  
 789 depletion. Due to a lack of data, we do not know whether this is a feature along the en-  
 790 tire boundary between the Rehoboth Terrane and Namaqua-Natal Belt or if it is lim-  
 791 ited to the area around the Gibeon kimberlite field.

## 792 5.7 Distribution of kimberlites

793 Kimberlites are hydrous and carbonated volcanic rocks that originate from low-degree  
 794 melting of the mantle below  $\sim 150$  km (Giuliani et al., 2020). Because they ascend very  
 795 rapidly ( $> 4$  to 20 m/s, Sparks et al., 2006) and entrain xenoliths and xenocrysts from

796 surrounding wall-rock, they provide an invaluable window to the deeper mantle. The cur-  
 797 rent most accepted mechanism for the faster ascent rates is crack-tip propagation via  $CO_2$   
 798 exsolution, in which carbonated melts cleave the mantle by carbon degassing at the top  
 799 of the percolation front while dissolving and assimilating orthopyroxene from the wall  
 800 rock (Russell et al., 2012; Giuliani et al., 2020).

801 Clifford’s rule (Clifford, 1966) suggests that diamondiferous kimberlites occur in  
 802 terranes with Archean crust. Today we know that diamondiferous kimberlites frequently  
 803 sample the cratonic mantle because diamonds are only stable below 130-150 km at colder  
 804 cratonic geotherms (Day, 2012). Temporally, the genesis of kimberlites is linked to ma-  
 805 jor tectonic events associated with global plate reorganisations such as the assembly and  
 806 disruption of Gondwana (Jelsma et al., 2009). Spatially, kimberlites are mostly restricted  
 807 to the edges of depleted cratonic keels comprised of chemically refertilised lithospheric  
 808 mantle (Griffin et al., 2009; Faure et al., 2011). This specific spatiotemporal distribu-  
 809 tion of the kimberlites is correlated with fossil and active tectonic boundaries (Jelsma  
 810 et al., 2004). These are commonly observed as lineaments in potential field geophysical  
 811 studies (Corner & Durrheim, 2018), possibly indicating the tendency of kimberlites to  
 812 use pre-existing zones of weakness in the lithosphere.

813 Through interpolated maximum resistivity maps of the lithospheric mantle, A. G. Jones  
 814 et al. (2009) showed that kimberlites in southern Africa tend to concentrate near the edges  
 815 of deep resistors that may correspond to depleted and dry cratonic keels. To compare  
 816 the distribution of kimberlites and our magnetotelluric models, we made maps of man-  
 817 tle conductance ( $\sum_{n=i}^n \sigma_i d_i$ ; i.e., integrated conductivity ( $\sigma$ ) times thickness ( $d$ )) between  
 818 50-150 km (Figure 11a). Another map (Figure 11b) shows where the greatest depth to  
 819 the 1000  $\Omega m$  value is observed. While containing similar information to the conductance  
 820 map, this map emphasizes the spatial distribution of thick resistive roots. These maps  
 821 demonstrate that kimberlites tend to be emplaced at the edges of the deepest and most  
 822 resistive parts of the cratonic lithospheric mantle while also avoiding the most conduc-  
 823 tive parts.

824 One reason for the distribution of kimberlites around the deep resistors might be  
 825 the inability of kimberlitic melts to penetrate thick and depleted cratonic roots. In such  
 826 depleted regions, the kimberlite magmas may react with the refractory wall-rock mate-  
 827 rials to the extent that they cannot ascend to the surface (Giuliani et al., 2016). If these  
 828 highly resistive keels have an orthopyroxene-poor (< 15%) dunitic composition as sug-  
 829 gested by some authors (e.g., Griffin et al., 2009), the rapid-ascent mechanism of crack-  
 830 tip propagation via  $CO_2$  degassing through assimilation of orthopyroxene from the wall  
 831 rock might not operate efficiently (Russell et al., 2012). Generation of kimberlitic melt  
 832 requires either the lithospheric mantle or the magma source beneath the lithosphere to  
 833 be enriched in volatiles. This could be possible via metasomatism and carbonate freez-  
 834 ing near the base of the lithosphere, including by Phanerozoic subduction processes (C. Sun  
 835 & Dasgupta, 2020). A recent study suggests that the enriched signatures observed in kimberlite-  
 836 hosted xenoliths globally reflect assimilated lithospheric mantle material (Giuliani et al.,  
 837 2020). These factors also make penetration of kimberlites through deep resistors less likely,  
 838 because higher water and carbon contents would be required to melt mantle peridotite  
 839 in keels that extend to greater depths (Foley & Pintér, 2018) and thick Archean cratonic  
 840 keels are unlikely to have been affected by subduction-related metasomatism. All of these  
 841 things considered, it is more likely for kimberlites to episodically erupt at places that have  
 842 previously been enriched in orthopyroxene, metasomatised and carbonated, and there-  
 843 fore have a moderate to low resistivity. Such events are more likely to concentrate around  
 844 fossil continent/micro-continent collision zones with metasomatised compositions, as sup-  
 845 ported by correlations of kimberlite occurrences with magnetic and geological lineaments  
 846 (Jelsma et al., 2004).

847 In the model, there are regions at the edges of the resistive roots ( $> 1000 \Omega m$ ) where  
 848 the lithospheric mantle has lower resistivities (100-1000  $\Omega m$ ) at depths greater than 100 km.

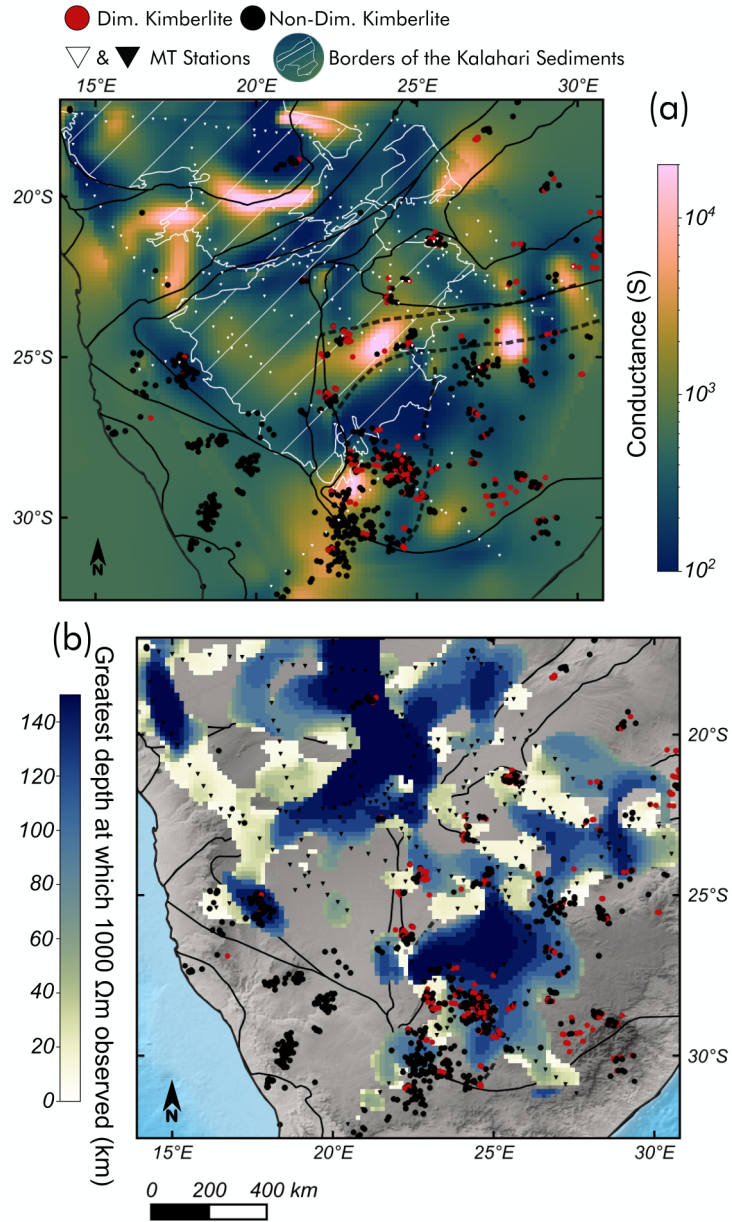


**Figure 11.** Distribution of kimberlites compared to (a) Lithospheric mantle conductance (from 50-200 km) and (b) The maximum depth at which a resistivity of  $1000 \Omega m$  is observed.

849 There are clear associations between these areas and kimberlite clusters (Figure 11) and  
 850 almost all diamondiferous kimberlites occur within these relatively conductive zones. These  
 851 conductive zones are indicated in Figure 11b as lighter blue areas usually appearing near  
 852 darker blue, thick resistive zones. In contrast, non-diamondiferous kimberlites can be ob-  
 853 served in these lower resistivity areas as well as in the more resistive portions of the cra-  
 854 tons. These lower-resistivity regions are likely to have gone through broad-scale meta-  
 855 somatism, as also shown by their garnet xenocryst geochemical 'tomography' (Figure 6)  
 856 and the compositions of whole-rock xenoliths, which include modal metasomatic min-  
 857 erals (e.g., Grégoire et al., 2003). Accordingly, a general recipe for diamond exploration  
 858 with magnetotelluric data would be to search for regions located between the resistors  
 859 of the cratonic nuclei and the conductors of metasomatised trans-lithospheric weakness  
 860 zones.

861 On the other hand, it is not clear why kimberlite clusters avoid the prominent man-  
 862 tle conductors around the resistive cratonic nuclei. Similar behaviour has also been ob-  
 863 served seismically, whereby kimberlites avoid regions of low shear wave velocity (Grif-  
 864 fin et al., 2009). To examine this question further, detailed descriptions of these conduc-  
 865 tors have to be considered. One example of a prominent mantle conductor is the one at  
 866 the southwest of the Kimberley area (SKC, Figure 2a,b). This conductor extends sub-  
 867 vertically towards the surface at the edge of the craton where the Kheis Orogenic Belt  
 868 and related fault systems are situated. This feature may be related to the collision be-  
 869 tween the proto-Namaqua-Natal Belt and the Kaapvaal Craton, and such conductors are  
 870 often observed along fossil and active suture zones (e.g., Kelbert et al., 2019; Kirkby et  
 871 al., 2020). Using the structural weakness corridor, Group I kimberlites may have further  
 872 mineralised this pathway with rising metasomatic fluids. If kimberlites preferentially as-  
 873 cend along pre-existing zones of lithospheric weakness (e.g., Jelsma et al., 2004), this would  
 874 be a perfect candidate. However, the area around this conductor contains only a few kim-  
 875 berlites, while most of the kimberlites in this region instead overlie relatively resistive  
 876 mantle.

877 The absence of kimberlites associated with the Molopo Farms and Bushveld com-  
 878 plex conductors may provide insight into the reasons kimberlites appear to avoid con-  
 879 ductors more generally. Since both mantle conductors are associated with large mafic  
 880 intrusions, one could argue that low-degree kimberlitic melts might have a rheological  
 881 preference to move laterally along the contact with the Transvaal Basin when they meet  
 882 the mafic material. This model could explain the near absence of kimberlites erupted  
 883 over these conductors. Another possibility might be that a very depleted mantle exists  
 884 near the base of the lithosphere ( $> 200$  km) due to melt pooling in large volumes at this  
 885 depth until it finally penetrates the lithospheric mantle. This model of Silver et al. (2006)  
 886 is suggested to explain the very short duration ( $< 1m.y.$ , Zeh et al., 2015) of emplace-  
 887 ment of the Bushveld Complex. In such a scenario, kimberlites might not be able to pen-  
 888 etrate this depleted layer or be generated within in due to low amounts of volatiles left  
 889 in the layer after this massive melt extraction (Figure 12), similar to emplacement be-  
 890 haviour observed at resistive cratonic nuclei.

## 891 6 Concluding Remarks and Summary

892 3D MT models of southern Africa and geochemical information from garnet xenocrysts  
 893 in Group I kimberlites are compared in the light of their tectonic and magmatic history.  
 894 Both qualitative and quantitative interpretations were made for MT-derived composi-  
 895 tion analysis. Some of the most critical discussion points are:

- 896 • No general relationships can be made between the age of the terranes and con-  
 897 ductivity distribution in the mantle since magmatic processes can either deplete  
 898 or refertilise the lithospheric mantle.

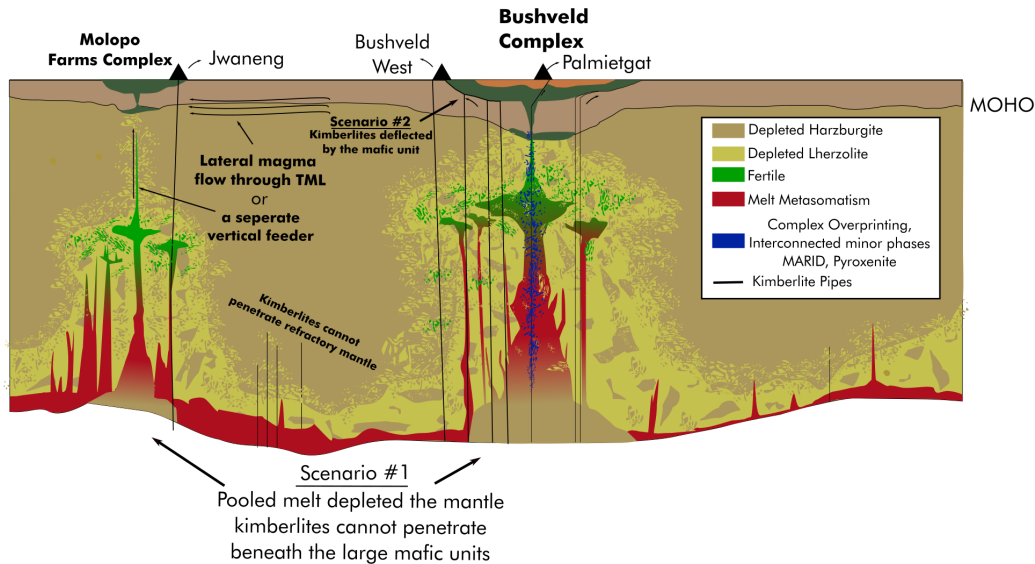


**Figure 12.** Conceptual sketch of our interpretation of mantle beneath the Bushveld Region. Scenarios 1 and 2 represents the possible reasons why kimberlites might avoid the center of the conductors. In Scenario 1, kimberlites avoid the conductors because they cannot penetrate or be generated within the depleted mantle formed by intense melt extraction during the Bushveld event. Scenario 2 posits the possibility that the kimberlites might be deflected by the mafic layer.

- 899
- 900
- 901
- 902
- 903
- 904
- 905
- 906
- 907
- 908
- 909
- 910
- 911
- 912
- 913
- 914
- 915
- 916
- 917
- 918
- 919
- 920
- 921
- 922
- 923
- 924
- 925
- Most of the Archean cratonic regions are imaged as relatively depleted regions with lower whole-rock  $Al_2O_3$  values, higher mean  $Mg^{ol}\#$ , and a lower proportion of metasomatised CARP classes between 100-150 km. Some Archean areas around the Bushveld and Molopo Farms complexes appear to have a more fertile signature and metasomatised characteristics, matching well with electrically conductive mantle the large-scale magmatic event that occurred at 2.05 Ga.
  - The area around the Bushveld Complex contains an increased proportion of unclassified garnets in the CARP classification scheme, suggesting either complex overprinting of multiple magmatic episodes. Conductivities below 100 km cannot be explained by water but can be explained by perfectly connected phlogopites. Conductivities above 100 km suggest that well-connected accessory minerals (e.g., sulfides, graphite or chromite) are likely to be present, precipitated extensively using the lithospheric weakness zone along the Thabazimbi-Murchison Lineament.
  - The electrical conductivity of the cratonic mantle reflects the style of metasomatism, i.e., the composition of metasomatic fluids, how they were emplaced and the extent of the metasomatism, rather than reflecting simply the fertility of the mantle peridotite. This is best exemplified by the lithospheric mantle in the vicinity of Gibeon Fields, which is geochemically fertile yet highly resistive.
  - Kimberlites in southern Africa are more likely to be observed around the edges of highly resistive mantle regions but also avoid the most conductive areas. They are most populous where the mantle below 100 km depth is relatively conductive. In resistive, depleted, orthopyroxene-poor and volatile-poor mantle, kimberlites are likely unable to penetrate through the mantle or cannot be generated.
  - Conductive regions with no co-located kimberlites are usually associated with a mafic intrusion (e.g., Bushveld Complex, Molopo Farms Complex). We suggest this is due to: (1) A rheological preference of kimberlitic melts to intrude the contact with the sedimentary units when they meet the mafic layer; and/or (2) dur-

926 ing an event like Bushveld magmatism, in which significant volumes of magma are  
 927 rapidly emplaced, volatiles near the lithosphere-asthenosphere boundary are also  
 928 intensively extracted, created a zone where kimberlites either cannot penetrate  
 929 or be generated.

## 930 Acronyms

931 **BC** Bushveld Complex  
 932 **BDL** Base of the Depleted Lithosphere  
 933 **CARP** Cluster Analysis by Regressive Partitioning  
 934 **LIP** Large Igneous Province  
 935 **MT** Magnetotelluric  
 936 **MARID** Mica-Amphibole-Rutile-Ilmenite-Diopside  
 937 **MFC** Molopo Farms Complex  
 938 **NAMs** Nominally Anhydrous Minerals  
 939 **PGE** Platinum-Group Elements  
 940 **REE** Rare-earth Elements  
 941 **SAMTEX** South African Magnetotelluric Experiment  
 942 **SHF** Surface Heat Flow  
 943 **TML** Thabazimbi-Murchison Lineament

## 944 Acknowledgments

945 This study was supported by Australian Research Council grant FT150100541. We thank  
 946 the SAMTEX team for making the SAMTEX magnetotelluric dataset available at the  
 947 IRIS SPUD repository (<https://doi.org/10.17611/DP/EMTF/SAMTEX>). We acknowl-  
 948 edge the research funds for the TARDIS Project provided by the ARC Centre of Excel-  
 949 lence for Core to Crust Fluid Systems (CCFS) and geochemical laboratory support through  
 950 NCRIS AuScope and NSW Government Research Attraction and Acceleration Program  
 951 grants. This is contribution XXX from the ARC Centre of Excellence for CCFS and YYY  
 952 from the GEMOC Key Centre.

## 953 References

- 954 Afonso, J. C., Fernández, M., Ranalli, G., Griffin, W. L., & Connolly, J. A. (2008).  
 955 Integrated geophysical-petrological modeling of the lithosphere and sublithospheric  
 956 upper mantle: Methodology and applications. *Geochemistry, Geophysics, Geosys-*  
 957 *tems*, 9(5). doi: 10.1029/2007GC001834
- 958 Alard, O., Griffin, W. L., Lorand, J. P., Jackson, S. E., & O'Reilly, S. Y. (2000).  
 959 Non-chondritic distribution of the highly siderophile elements in mantle sulphides.  
 960 *Nature*, 407(6806), 891–894.
- 961 Amante, C., & Eakins, B. (2009). Etopo1 1 arc-minute global relief model: proce-  
 962 dures, data sources and analysis. noaa technical memorandum nesdis ngdc-24. *Na-*  
 963 *tional Geophysical Data Center, NOAA*, 10, V5C8276M.
- 964 Begg, G. C., Hronsky, J. A., Arndt, N. T., Griffin, W. L., O'Reilly, S. Y., &  
 965 Hayward, N. (2010). Lithospheric, cratonic, and geodynamic setting of  
 966 Ni-Cu-PGE sulfide deposits. *Economic Geology*, 105(6), 1057–1070. doi:  
 967 10.2113/econgeo.105.6.1057
- 968 Bell, D. R., Ihinger, P. D., & Rossman, G. R. (1995, jun). Quantitative analysis of  
 969 trace OH in garnet and pyroxenes. *American Mineralogist*, 80(5-6), 465–474. doi:  
 970 10.2138/am-1995-5-607
- 971 Bell, D. R., Schmitz, M. D., & Janney, P. E. (2003). Mesozoic thermal evolution of

- 972 the southern African mantle lithosphere. *Lithos*, *71*(2-4), 273–287. doi: 10.1016/  
 973 S0024-4937(03)00117-8
- 974 Beukes, N. J., de Kock, M. O., Vorster, C., Ravhura, L. G., Frei, D., Gumsley, A. P.,  
 975 & Harris, C. (2019). The age and country rock provenance of the Molopo farms  
 976 complex: Implications for transvaal supergroup correlation in southern Africa.  
 977 *South African Journal of Geology*, *122*(1), 39–56. doi: 10.25131/sajg.122.0003
- 978 Brey, G., & Köhler, T. (1990). Geothermobarometry in four-phase lherzolites ii. new  
 979 thermobarometers, and practical assessment of existing thermobarometers. *Jour-  
 980 nal of Petrology*, *31*(6), 1353–1378. doi: 10.1016/0016-7037(90)90226-B
- 981 Cawthorn, R. G. (2015). The bushveld complex, south africa. In *Layered intrusions*  
 982 (pp. 517–587). Springer.
- 983 Chisenga, C., Jianguo, Y., Fadel, I., van der Meijde, M., & Atekwana, E. A. (2020).  
 984 Updated tectonic terrane boundaries of Botswana determined from gravity and  
 985 aeromagnetic data. *Episodes*, *43*(4), 919–933. doi: 10.18814/EPIIUGS/2020/  
 986 020054
- 987 Clarke, B., Uken, R., & Reinhardt, J. (2009). Structural and compositional con-  
 988 straints on the emplacement of the Bushveld Complex, South Africa. *Lithos*,  
 989 *111*(1-2), 21–36. doi: 10.1016/j.lithos.2008.11.006
- 990 Clifford, T. N. (1966). Tectono-metallogenic units and metallogenic provinces of  
 991 Africa. *Earth and Planetary Science Letters*, *1*(6), 421–434. doi: 10.1016/0012-  
 992 -821X(66)90039-2
- 993 Cole, J., Webb, S. J., & Finn, C. A. (2014). Gravity models of the Bushveld Com-  
 994 plex - Have we come full circle? *Journal of African Earth Sciences*, *92*, 97–118.  
 995 doi: 10.1016/j.jafrearsci.2014.01.012
- 996 Corner, B., & Durrheim, R. J. (2018). An integrated geophysical and geological in-  
 997 terpretation of the southern african lithosphere. In *Geology of southwest gondwana*  
 998 (pp. 19–61). Springer.
- 999 Dai, L., Hu, H., Sun, W., Li, H., Liu, C., & Wang, M. (2019). Influence of high con-  
 1000 ductive magnetite impurity on the electrical conductivity of dry olivine aggregates  
 1001 at high temperature and high pressure. *Minerals*, *9*(1). doi: 10.3390/min9010044
- 1002 Dai, L., & Karato, S.-i. (2009a). Electrical conductivity of orthopyroxene: Im-  
 1003 plications for the water content of the asthenosphere. *Proceedings of the Japan*  
 1004 *Academy, Series B*, *85*(10), 466–475. doi: 10.2183/pjab.85.466
- 1005 Dai, L., & Karato, S.-i. (2009b). Electrical conductivity of pyrope-rich garnet at  
 1006 high temperature and high pressure. *Physics of the Earth and Planetary Interiors*,  
 1007 *176*(1-2), 83–88. doi: 10.1016/j.pepi.2009.04.002
- 1008 Dai, L., & Karato, S.-i. (2014). High and highly anisotropic electrical conductivity of  
 1009 the asthenosphere due to hydrogen diffusion in olivine. *Earth and Planetary Sci-  
 1010 ence Letters*, *408*, 79–86. doi: 10.1016/j.epsl.2014.10.003
- 1011 Davies, G. R., Spriggs, A. J., & Nixon, P. H. (2001). A non-cognate origin  
 1012 for the Gibeon kimberlite megacryst suite, Namibia: Implications for the ori-  
 1013 gin of Namibian kimberlites. *Journal of Petrology*, *42*(1), 159–172. doi:  
 1014 10.1093/petrology/42.1.159
- 1015 Davis, G. L. (1977). The ages and uranium contents of zircons from kimberlites  
 1016 and associated rocks. In *International kimberlite conference: Extended abstracts*  
 1017 (Vol. 2, pp. 67–69).
- 1018 Dawson, J. B., & Stephens, W. (1975). Statistical classification of garnets from kim-  
 1019 berlite and associated xenoliths. *The Journal of Geology*, *83*(5), 589–607.
- 1020 Day, H. W. (2012). A revised diamond-graphite transition curve. *American Mineral-  
 1021 ogist*, *97*(1), 52–62. doi: 10.2138/am.2011.3763
- 1022 De Kock, M. O., Ernst, R., Söderlund, U., Jourdan, F., Hofmann, A., Le Gall, B.,  
 1023 ... Fuchs, R. (2014). Dykes of the 1.11Ga Umkondo LIP, Southern Africa:  
 1024 Clues to a complex plumbing system. *Precambrian Research*, *249*, 129–143. doi:  
 1025 10.1016/j.precamres.2014.05.006

- 1026 De Wit, M. J., De Ronde, C. E., Tredoux, M., Roering, C., Hart, R. J., Armstrong,  
1027 R. A., ... Hart, R. A. (1992, jun). Formation of an Archaean continent. *Nature*,  
1028 *357*(6379), 553–562. doi: 10.1038/357553a0
- 1029 De Beer, J. H. (2016). *The history of geophysics in southern africa*. African Sun Me-  
1030 dia.
- 1031 Delph, J. R., & Porter, R. C. (2015). Crustal structure beneath southern Africa:  
1032 Insight into how tectonic events affect the Mohorovičić discontinuity. *Geophysical*  
1033 *Journal International*, *200*(1), 254–264. doi: 10.1093/gji/ggu376
- 1034 Demouchy, S., & Bolfan-Casanova, N. (2016). Distribution and transport of hydro-  
1035 gen in the lithospheric mantle: A review. *Lithos*, *240-243*, 402–425. doi: 10.1016/  
1036 j.lithos.2015.11.012
- 1037 Demouchy, S., Shcheka, S., Denis, C. M., & Thoraval, C. (2017). Subsolidus hy-  
1038 drogen partitioning between nominally anhydrous minerals in garnet-bearing peri-  
1039 dotite. *American Mineralogist*, *102*(9), 1822–1831. doi: 10.2138/am-2017-6089
- 1040 Evans, R. L., Jones, A. G., Garcia, X., Muller, M., Hamilton, M., Evans, S., ...  
1041 Hutchins, D. (2011). Electrical lithosphere beneath the Kaapvaal craton, south-  
1042 ern Africa. *Journal of Geophysical Research: Solid Earth*, *116*(4), 1–16. doi:  
1043 10.1029/2010JB007883
- 1044 Faure, S., Godey, S., Fallara, F., & Trépanier, S. (2011). Seismic architecture of the  
1045 archaean north american mantle and its relationship to diamondiferous kimberlite  
1046 fields. *Economic Geology*, *106*(2), 223–240. doi: 10.2113/econgeo.106.2.223
- 1047 Férot, A., & Bolfan-Casanova, N. (2012). Water storage capacity in olivine and  
1048 pyroxene to 14GPa: Implications for the water content of the Earth’s upper man-  
1049 tle and nature of seismic discontinuities. *Earth and Planetary Science Letters*,  
1050 *349-350*, 218–230. doi: 10.1016/j.epsl.2012.06.022
- 1051 Foley, S. F. (1992). Vein-plus-wall-rock melting mechanisms in the lithosphere and  
1052 the origin of potassic alkaline magmas. *Lithos*, *28*(3-6), 435–453. doi: 10.1016/  
1053 0024-4937(92)90018-T
- 1054 Foley, S. F., & Pintér, Z. (2018). *Primary Melt Compositions in the Earth’s Mantle*.  
1055 doi: 10.1016/B978-0-12-811301-1.00001-0
- 1056 Fouch, M. J., James, D. E., VanDecar, J. C., & van der Lee, S. (2004). Mantle seis-  
1057 mic structure beneath the Kaapvaal and Zimbabwe Cratons. *South African Jour-  
1058 nal of Geology*, *107*(1-2), 33–44. doi: 10.2113/107.1-2.33
- 1059 Gardés, E., Gaillard, F., & Tarits, P. (2014, dec). Toward a unified hydrous olivine  
1060 electrical conductivity law. *Geochemistry, Geophysics, Geosystems*, *15*(12), 4984–  
1061 5000. Retrieved from <http://doi.wiley.com/10.1002/2014GC005496> doi: 10  
1062 .1002/2014GC005496
- 1063 Gaul, O. F., Griffin, W. L., O’Reilly, S. Y., & Pearson, N. J. (2000). Mapping  
1064 olivine composition in the lithospheric mantle. *Earth and Planetary Science*  
1065 *Letters*, *182*(3-4), 223–235. doi: 10.1016/S0012-821X(00)00243-0
- 1066 Giuliani, A., Graham Pearson, D., Soltys, A., Dalton, H., Phillips, D., Foley, S. F.,  
1067 ... Mitchell, R. H. (2020). Kimberlite genesis from a common carbonate-rich pri-  
1068 mary melt modified by lithospheric mantle assimilation. *Science Advances*, *6*(17),  
1069 1–10. doi: 10.1126/sciadv.aaz0424
- 1070 Giuliani, A., Phillips, D., Kamenetsky, V. S., & Goemann, K. (2016). Con-  
1071 straints on kimberlite ascent mechanisms revealed by phlogopite compositions  
1072 in kimberlites and mantle xenoliths. *Lithos*, *240-243*(2016), 189–201. doi:  
1073 10.1016/j.lithos.2015.11.013
- 1074 Giuliani, A., Phillips, D., Woodhead, J. D., Kamenetsky, V. S., Fiorentini, M. L.,  
1075 Maas, R., ... Armstrong, R. A. (2015). Did diamond-bearing orangeites originate  
1076 from MARID-veined peridotites in the lithospheric mantle? *Nature Communica-  
1077 tions*, *6*. doi: 10.1038/ncomms7837
- 1078 Glover, P. W. J. (2010). A generalized Archie’s law for n phases. *Geophysics*, *75*(6),  
1079 E247–E265. doi: 10.1190/1.3509781

- 1080 Good, N., & De Wit, M. J. (1997). The Thabazimbi-Murchison lineament of the  
 1081 Kaapvaal Craton, South Africa: 2700 Ma of episodic deformation. *Journal of the*  
 1082 *Geological Society*, *154*(1), 93–97. doi: 10.1144/gsjgs.154.1.0093
- 1083 Goscombe, B., Foster, D. A., Gray, D., Wade, B., Marsellos, A., & Titus, J. (2017).  
 1084 Deformation correlations, stress field switches and evolution of an orogenic inter-  
 1085 section: The Pan-African Kaoko-Damara orogenic junction, Namibia. *Geoscience*  
 1086 *Frontiers*, *8*(6), 1187–1232. doi: 10.1016/j.gsf.2017.05.001
- 1087 Grégoire, M., Bell, D. R., & Le Roex, A. P. (2003). Garnet lherzolites from the  
 1088 Kaapvaal Craton (South Africa): Trace element evidence for a metasomatic his-  
 1089 tory. *Journal of Petrology*, *44*(4), 629–657. doi: 10.1093/petrology/44.4.629
- 1090 Griffin, W. L., Begg, G. C., & O’Reilly, S. Y. (2013). Continental-root control on  
 1091 the genesis of magmatic ore deposits. *Nature Geoscience*, *6*(11), 905–910. doi: 10  
 1092 .1038/ngeo1954
- 1093 Griffin, W. L., Fisher, N. I., Friedman, J. H., O’Reilly, S. Y., & Ryan, C. G. (2002).  
 1094 Cr-pyrope garnets in the lithospheric mantle 2. Compositional populations and  
 1095 their distribution in time and space. *Geochemistry, Geophysics, Geosystems*,  
 1096 *3*(12), 1–35. doi: 10.1029/2002gc000298
- 1097 Griffin, W. L., O’Reilly, S. Y., Afonso, J. C., & Begg, G. C. (2009). The composition  
 1098 and evolution of lithospheric mantle: A re-evaluation and its tectonic implications.  
 1099 *Journal of Petrology*, *50*(7), 1185–1204. doi: 10.1093/petrology/egn033
- 1100 Griffin, W. L., O’Reilly, S. Y., Natapov, L. M., & Ryan, C. G. (2003). The evolution  
 1101 of lithospheric mantle beneath the Kalahari Craton and its margins. *Lithos*, *71*(2-  
 1102 4), 215–241. doi: 10.1016/j.lithos.2003.07.006
- 1103 Griffin, W. L., Shee, S. R., Ryan, C. G., Win, T. T., & Wyatt, B. A. (1999).  
 1104 Harzburgite to lherzolite and back again: metasomatic processes in ultramafic  
 1105 xenoliths from the Wesselton kimberlite, Kimberley, South Africa. *Contrib Min-  
 1106 eral Petrol*, *134*, 232–250.
- 1107 Grütter, H. S., Gurney, J. J., Menzies, A. H., & Winter, F. (2004). An updated clas-  
 1108 sification scheme for mantle-derived garnet, for use by diamond explorers. *Lithos*,  
 1109 *77*(1-4), 841–857.
- 1110 Gumsley, A., Stamsnijder, J., Larsson, E., Söderlund, U., Naeraa, T., De Kock, M.,  
 1111 ... Ernst, R. (2020). Neoproterozoic large igneous provinces on the Kaapvaal Craton  
 1112 in southern Africa re-define the formation of the Ventersdorp Supergroup and its  
 1113 temporal equivalents. *Bulletin of the Geological Society of America*, *132*(9-10),  
 1114 1829–1844. doi: 10.1130/B35237.1
- 1115 Hanson, R. E. (2003). Proterozoic geochronology and tectonic evolution of southern  
 1116 Africa. *Geological Society Special Publication*, *206*, 427–463.
- 1117 Hanson, R. E., Harmer, R. E., Blenkinsop, T. G., Bullen, D. S., Dalziel, I. W., Gose,  
 1118 W. A., ... Ward, S. E. (2006). Mesoproterozoic intraplate magmatism in the  
 1119 Kalahari Craton: A review. *Journal of African Earth Sciences*, *46*(1-2), 141–167.  
 1120 doi: 10.1016/j.jafrearsci.2006.01.016
- 1121 Hasterok, D., & Chapman, D. S. (2011). Heat production and geotherms for the  
 1122 continental lithosphere. *Earth and Planetary Science Letters*, *307*(1-2), 59–70.  
 1123 doi: 10.1016/j.epsl.2011.04.034
- 1124 Humbert, F., de Kock, M., Lenhardt, N., & Altermann, W. (2019). Neoproterozoic to  
 1125 early palaeoproterozoic within-plate volcanism of the kaapvaal craton: Comparing  
 1126 the ventersdorp supergroup and the ongeluk and hekpoort formations (transvaal  
 1127 supergroup). In *The archaean geology of the kaapvaal craton, southern africa* (pp.  
 1128 277–302). Springer.
- 1129 Jacobs, J., Pisarevsky, S., Thomas, R. J., & Becker, T. (2008). The Kalahari Cra-  
 1130 ton during the assembly and dispersal of Rodinia. *Precambrian Research*, *160*(1-  
 1131 2), 142–158. doi: 10.1016/j.precamres.2007.04.022
- 1132 Jelsma, H. A., Barnett, W., Richards, S., & Lister, G. (2009). Tectonic setting of  
 1133 kimberlites. *Lithos*, *112*, 155–165. doi: 10.1016/j.lithos.2009.06.030

- 1134 Jelsma, H. A., de Wit, M. J., Thiar, C., Dirks, P. H., Viola, G., Basson, I. J., &  
 1135 Anckar, E. (2004). Preferential distribution along transcontinental corridors  
 1136 of kimberlites and related rocks of Southern Africa. *South African Journal of*  
 1137 *Geology*, *107*(1-2), 301–324. doi: 10.2113/107.1-2.301
- 1138 Jones, A. G., Evans, R. L., Muller, M. R., Hamilton, M. P., Miensopust, M. P.,  
 1139 Garcia, X., . . . Wasborg, J. (2009). Area selection for diamonds using mag-  
 1140 netotellurics: Examples from southern Africa. *Lithos*, *112*, 83–92. doi:  
 1141 10.1016/j.lithos.2009.06.011
- 1142 Jones, M. (2017). Heat flow in the Bushveld Complex, South Africa: implications for  
 1143 upper mantle structure. *South African Journal of Geology*, *120*(3), 351–370. doi:  
 1144 10.25131/gssajg.120.3.351
- 1145 Jourdan, F., Féraud, G., Bertrand, H., Watkeys, M. K., Kampunzu, A. B., &  
 1146 Le Gall, B. (2006). Basement control on dyke distribution in Large Igneous  
 1147 Provinces: Case study of the Karoo triple junction. *Earth and Planetary Science*  
 1148 *Letters*, *241*(1-2), 307–322. doi: 10.1016/j.epsl.2005.10.003
- 1149 Kaavera, J., Rajesh, H. M., Tsunogae, T., & Belyanin, G. A. (2018). Marginal  
 1150 facies and compositional equivalents of Bushveld parental sills from the Molopo  
 1151 Farms Complex layered intrusion, Botswana: Petrogenetic and mineraliza-  
 1152 tion implications. *Ore Geology Reviews*, *92*(November 2017), 506–528. doi:  
 1153 10.1016/j.oregeorev.2017.12.001
- 1154 Karato, S.-i., & Wang, D. (2012). Electrical conductivity of minerals and rocks.  
 1155 *Physics and Chemistry of the Deep Earth*, 145–236.
- 1156 Kelbert, A., Bedrosian, P. A., & Murphy, B. S. (2019). The first 3D conductivity  
 1157 model of the contiguous United States: Reflections on geologic structure and ap-  
 1158 plication to induction hazards. *Geomagnetically Induced Currents from the Sun to*  
 1159 *the Power Grid*, 127–151. doi: 10.1002/9781119434412.ch8
- 1160 Kelbert, A., Meqbel, N., Egbert, G. D., & Tandon, K. (2014). ModEM: A modu-  
 1161 lar system for inversion of electromagnetic geophysical data. *Computers and Geo-*  
 1162 *sciences*, *66*, 40–53. doi: 10.1016/j.cageo.2014.01.010
- 1163 Kgaswane, E. M., Nyblade, A. A., Durrheim, R. J., Julià, J., Dirks, P. H. G. M., &  
 1164 Webb, S. J. (2012). Shear wave velocity structure of the Bushveld Complex, South  
 1165 Africa. *Tectonophysics*, *554-557*, 83–104. doi: 10.1016/j.tecto.2012.06.003
- 1166 Khoza, D., Jones, A. G., Muller, M. R., Evans, R. L., Miensopust, M. P., & Webb,  
 1167 S. J. (2013a). Lithospheric structure of an Archean craton and adjacent mobile  
 1168 belt revealed from 2-D and 3-D inversion of magnetotelluric data: Example from  
 1169 southern Congo craton in northern Namibia. *Journal of Geophysical Research:*  
 1170 *Solid Earth*, *118*(8), 4378–4397. doi: 10.1002/jgrb.50258
- 1171 Khoza, D., Jones, A. G., Muller, M. R., Evans, R. L., Webb, S. J., & Mienso-  
 1172 pust, M. (2013b). Tectonic model of the Limpopo belt: Constraints from  
 1173 magnetotelluric data. *Precambrian Research*, *226*, 143–156. doi: 10.1016/  
 1174 j.precamres.2012.11.016
- 1175 Kirkby, A. L., Musgrave, R. J., Czarnota, K., Doublier, M. P., Duan, J., Cayley,  
 1176 R. A., & Kyi, D. (2020). Lithospheric architecture of a Phanerozoic orogen from  
 1177 magnetotellurics: AusLAMP in the Tasmanides, southeast Australia. *Tectono-*  
 1178 *physics*, *793*(November 2019), 228560. doi: 10.1016/j.tecto.2020.228560
- 1179 Kobussen, A. F., Griffin, W. L., & O’Reilly, S. Y. (2009). Cretaceous thermo-  
 1180 chemical modification of the Kaapvaal cratonic lithosphere, South Africa. *Lithos*,  
 1181 *112*, 886–895. doi: 10.1016/j.lithos.2009.06.031
- 1182 Kobussen, A. F., Griffin, W. L., O’Reilly, S. Y., & Shee, S. R. (2008). Ghosts of  
 1183 lithospheres past: Imaging an evolving lithospheric mantle in southern Africa. *Ge-*  
 1184 *ology*, *36*(7), 515–518. doi: 10.1130/G24868A.1
- 1185 Kruger, F. J. (2005). Filling the Bushveld Complex magma chamber: Lateral ex-  
 1186 pansion, roof and floor interaction, magmatic unconformities, and the formation  
 1187 of giant chromitite, PGE and Ti-V-magnetitite deposits. *Mineralium Deposita*,

- 1188 40(5), 451–472. doi: 10.1007/s00126-005-0016-8
- 1189 Laurent, O., Zeh, A., Brandl, G., Vezinet, A., & Wilson, A. (2019). Granitoids and  
1190 greenstone belts of the pietersburg block—witnesses of an archaean accretionary  
1191 orogen along the northern edge of the kaapvaal craton. In *The archaean geology of*  
1192 *the kaapvaal craton, southern africa* (pp. 83–107). Springer.
- 1193 Li, A., & Burke, K. (2006). Upper mantle structure of southern Africa from  
1194 Rayleigh wave tomography. *Journal of Geophysical Research: Solid Earth*,  
1195 111(10), 1–16. doi: 10.1029/2006JB004321
- 1196 Li, Y., Jiang, H., & Yang, X. (2017). Fluorine follows water: Effect on electrical  
1197 conductivity of silicate minerals by experimental constraints from phlogopite.  
1198 *Geochimica et Cosmochimica Acta*, 217, 16–27. doi: 10.1016/j.gca.2017.08.020
- 1199 Liu, H., Zhu, Q., & Yang, X. (2019). Electrical conductivity of OH-bearing  
1200 omphacite and garnet in eclogite: the quantitative dependence on water con-  
1201 tent. *Contributions to Mineralogy and Petrology*, 174(7), 1–15. doi: 10.1007/  
1202 s00410-019-1593-3
- 1203 Maier, W. D., Peltonen, P., Grantham, G., & Mänttari, I. (2003). A new 1.9 Ga age  
1204 for the Trompsburg intrusion, South Africa. *Earth and Planetary Science Letters*,  
1205 212(3-4), 351–360. doi: 10.1016/S0012-821X(03)00281-4
- 1206 Master, S., Bekker, A., & Hofmann, A. (2010). A review of the stratigraphy and  
1207 geological setting of the Palaeoproterozoic Magondi Supergroup, Zimbabwe - Type  
1208 locality for the Lomagundi carbon isotope excursion. *Precambrian Research*,  
1209 182(4), 254–273. doi: 10.1016/j.precamres.2010.08.013
- 1210 McCourt, S., Armstrong, R. A., Jelsma, H., & Mapeo, R. B. (2013). New U-Pb  
1211 SHRIMP ages from the Lubango region, SW Angola: Insights into the Palaeopro-  
1212 terozoic evolution of the Angolan Shield, southern Congo Craton, Africa. *Journal*  
1213 *of the Geological Society*, 170(2), 353–363. doi: 10.1144/jgs2012-059
- 1214 Miensopust, M. P., Jones, A. G., Muller, M. R., Garcia, X., & Evans, R. L. (2011).  
1215 Lithospheric structures and Precambrian terrane boundaries in northeastern  
1216 Botswana revealed through magnetotelluric profiling as part of the Southern  
1217 African Magnetotelluric Experiment. *Journal of Geophysical Research: Solid*  
1218 *Earth*, 116(2), 1–21. doi: 10.1029/2010JB007740
- 1219 Modie, B. N. (2000). Geology and mineralisation in the meso-to neoproterozoic  
1220 ghanzi-chobe belt of northwest botswana. *Journal of African Earth Sciences*,  
1221 30(3), 467–474.
- 1222 Moorkamp, M., Fishwick, S., Walker, R. J., & Jones, A. G. (2019). Geophysical  
1223 evidence for crustal and mantle weak zones controlling intra-plate seismicity – the  
1224 2017 Botswana earthquake sequence. *Earth and Planetary Science Letters*, 506,  
1225 175–183. doi: 10.1016/j.epsl.2018.10.048
- 1226 Moorkamp, M., Heincke, B., Jegen, M., Roberts, A. W., & Hobbs, R. W. (2011). A  
1227 framework for 3-d joint inversion of mt, gravity and seismic refraction data. *Geo-*  
1228 *physical Journal International*, 184(1), 477–493.
- 1229 Moorkamp, M., Özaydın, S., Selway, K., Griffin, W., & Jones, A. G. (2021). A large  
1230 scale conductivity model for southern africa. *Journal of Geophysical Research:*  
1231 *Solid Earth*, submitted.
- 1232 Muller, M. R., Jones, A. G., Evans, R. L., Grütter, H. S., Hatton, C., Garcia,  
1233 X., ... Wasborg, J. (2009). Lithospheric structure, evolution and diamond  
1234 prospectivity of the Rehoboth Terrane and western Kaapvaal Craton, southern  
1235 Africa: Constraints from broadband magnetotellurics. *Lithos*, 112, 93–105. doi:  
1236 10.1016/j.lithos.2009.06.023
- 1237 Nimis, P., & Taylor, W. R. (2000). Single clinopyroxene thermobarometry for gar-  
1238 net peridotites. part i. calibration and testing of a cr-in-cpx barometer and an  
1239 enstatite-in-cpx thermometer. *Contributions to Mineralogy and Petrology*, 139(5),  
1240 541–554.
- 1241 Novella, D., Frost, D. J., Hauri, E. H., Bureau, H., Raepsaet, C., & Roberge, M.

- 1242 (2014). The distribution of H<sub>2</sub>O between silicate melt and nominally anhydrous  
 1243 peridotite and the onset of hydrous melting in the deep upper mantle. *Earth and*  
 1244 *Planetary Science Letters*, *400*, 1–13. doi: 10.1016/j.epsl.2014.05.006
- 1245 O’Reilly, S. Y., & Griffin, W. (2006). Imaging global chemical and thermal het-  
 1246 erogeneity in the subcontinental lithospheric mantle with garnets and xenoliths:  
 1247 Geophysical implications. *Tectonophysics*, *416*(1-4), 289–309.
- 1248 O’Reilly, S. Y., & Griffin, W. (2013). Moho vs crust–mantle boundary: evolution of  
 1249 an idea. *Tectonophysics*, *609*, 535–546.
- 1250 Oriolo, S., & Becker, T. (2018). The kalahari craton, southern africa: from archean  
 1251 crustal evolution to gondwana amalgamation. In *Geology of southwest gondwana*  
 1252 (pp. 133–159). Springer.
- 1253 Ortiz, K., Nyblade, A., van der Meijde, M., Paulssen, H., Kwadiba, M., Ntibinyane,  
 1254 O., . . . Homman, K. (2019). Upper Mantle P and S Wave Velocity Structure  
 1255 of the Kalahari Craton and Surrounding Proterozoic Terranes, Southern Africa.  
 1256 *Geophysical Research Letters*, *46*(16), 9509–9518. doi: 10.1029/2019GL084053
- 1257 Özaydın, S., & Selway, K. (2020). MATE: An analysis tool for the interpretation of  
 1258 magnetotelluric models of the mantle. *Geochemistry, Geophysics, Geosystems*, 1–  
 1259 26. doi: 10.1029/2020gc009126
- 1260 Özaydın, S., Selway, K., & Griffin, W. L. (2021). Are xenoliths from south-  
 1261 western Kaapvaal Craton representative of the broader mantle? Constraints  
 1262 from magnetotelluric modeling. *Geophysical Research Letters*, *48*, 1-11. doi:  
 1263 10.1029/2021GL092570
- 1264 Padrón-Navarta, J. A., & Hermann, J. (2017). A Subsolidus Olivine Water Sol-  
 1265 ubility Equation for the Earth’s Upper Mantle. *Journal of Geophysical Research:*  
 1266 *Solid Earth*, *122*(12), 9862–9880. doi: 10.1002/2017JB014510
- 1267 Palme, H., & O’Neill, H. (2013). *Cosmochemical Estimates of Mantle Composition*  
 1268 (2nd ed., Vol. 3). Elsevier Ltd. doi: 10.1016/B978-0-08-095975-7.00201-1
- 1269 Pearson, D. G., Boyd, F. R., Haggerty, S. E., Pasteris, J. D., Field, S. W., Nixon,  
 1270 P. H., & Pokhilenko, N. P. (1994). The characterisation and origin of graphite  
 1271 in cratonic lithospheric mantle: a petrological carbon isotope and Raman spectro-  
 1272 scopic study. *Contributions to Mineralogy and Petrology*, *115*(4), 449–466. doi:  
 1273 10.1007/BF00320978
- 1274 Pearson, D. G., Irvine, G. J., Ionov, D. A., Boyd, F. R., & Dreibus, G. E. (2004).  
 1275 Re-Os isotope systematics and platinum group element fractionation during man-  
 1276 tle melt extraction: A study of massif and xenolith peridotite suites. *Chemical*  
 1277 *Geology*, *208*(1-4), 29–59. doi: 10.1016/j.chemgeo.2004.04.005
- 1278 Pujol, M., Robb, L. J., Anhaeusser, C. R., & Gericke, B. (2003). A review  
 1279 of the geochronological constraints on the evolution of the Kaapvaal Cra-  
 1280 ton, South Africa. *Precambrian Research*, *127*(1-3), 181–213. doi: 10.1016/  
 1281 S0301-9268(03)00187-6
- 1282 Prendergast, M. D. (2012). The molopo farms complex, southern botswana - A re-  
 1283 consideration of structure, evolution, and the bushveld connection. *South African*  
 1284 *Journal of Geology*, *115*(1), 77–90. doi: 10.2113/gssajg.115.1.77
- 1285 Preston, R., & Sweeney, R. (2003). A comparison of clinopyroxene thermobaromet-  
 1286 ric techniques: applied to jwaneng, orapa and markt kimberlites. In *International*  
 1287 *kimberlite conference: Extended abstracts* (Vol. 8).
- 1288 Rajesh, H. M., Chisonga, B. C., Shindo, K., Beukes, N. J., & Armstrong, R. A.  
 1289 (2013). Petrographic, geochemical and SHRIMP U-Pb titanite age characteriza-  
 1290 tion of the Thabazimbi mafic sills: Extended time frame and a unifying petroge-  
 1291 netic model for the Bushveld Large Igneous Province. *Precambrian Research*, *230*,  
 1292 79–102. doi: 10.1016/j.precamres.2013.02.002
- 1293 Ravenna, M., Lebedev, S., Fullea, J., & Adam, J. M. (2018). Shear-Wave Velocity  
 1294 Structure of Southern Africa’s Lithosphere: Variations in the Thickness and Com-  
 1295 position of Cratons and Their Effect on Topography. *Geochemistry, Geophysics,*

- 1296 *Geosystems*, 19(5), 1499–1518. doi: 10.1029/2017GC007399
- 1297 Rezaie, M., Moradzadeh, A., Kalate, A. N., Aghajani, H., Kahoo, A. R., & Moazam,  
1298 S. (2017). 3D modelling of Trompsburg Complex (in South Africa) using 3D  
1299 focusing inversion of gravity data. *Journal of African Earth Sciences*, 130, 1–7.  
1300 doi: 10.1016/j.jafrearsci.2017.03.002
- 1301 Richardson, S. H., & Shirey, S. B. (2008). Continental mantle signature of  
1302 Bushveld magmas and coeval diamonds. *Nature*, 453(7197), 910–913. doi:  
1303 10.1038/nature07073
- 1304 Russell, J. K., Porritt, L. A., Lavallée, Y., & Dingwell, D. B. (2012). Kimberlite as-  
1305 cent by assimilation-fuelled buoyancy. *Nature*, 481(7381), 352–356.
- 1306 Ryan, C. G., Griffin, W. L., & Pearson, N. J. (1996). Garnet geotherms: Pressure-  
1307 temperature data from Cr-pyrope garnet xenocrysts in volcanic rocks. *Journal of*  
1308 *Geophysical Research: Solid Earth*, 101(B3), 5611–5625. doi: 10.1029/95JB03207
- 1309 Schmitz, M. D., & Bowring, S. A. (2004). Lower crustal granulite formation dur-  
1310 ing Mesoproterozoic Namaqua-Natal collisional orogenesis, southern Africa. *South*  
1311 *African Journal of Geology*, 107(1-2), 261–284. doi: 10.2113/107.1-2.261
- 1312 Scoates, J. S., Wall, C. J., Friedman, R. M., Weis, D., Mathez, E. A., & VanTon-  
1313 geren, J. A. (2021). Dating the Bushveld Complex: Timing of Crystallization,  
1314 Duration of Magmatism, and Cooling of the World’s Largest Layered Intrusion  
1315 and Related Rocks. *Journal of Petrology*(604). doi: 10.1093/petrology/egaa107
- 1316 Selway, K. (2015). Negligible effect of hydrogen content on plate strength in East  
1317 Africa. *Nature Geoscience*, 8(7), 543–546. doi: 10.1038/ngeo2453
- 1318 Selway, K., Hand, M., Payne, J. L., Heinson, G. S., & Reid, a. (2011). Mag-  
1319 netotelluric constraints on the tectonic setting of Grenville-aged orogenesis  
1320 in central Australia. *Journal of the Geological Society*, 168, 251–264. doi:  
1321 10.1144/0016-76492010-034
- 1322 Selway, K., O’Donnell, J. P., & Özyaydin, S. (2019, jul). Upper Mantle Melt Distribu-  
1323 tion From Petrologically Constrained Magnetotellurics. *Geochemistry, Geophysics,*  
1324 *Geosystems*, 2019GC008227. doi: 10.1029/2019GC008227
- 1325 Shu, Q., Brey, G. P., Gerdes, A., & Hofer, H. E. (2014). Mantle eclogites and gar-  
1326 net pyroxenites - the meaning of two-point isochrons, Sm-Nd and Lu-Hf closure  
1327 temperatures and the cooling of the subcratonic mantle. *Earth and Planetary*  
1328 *Science Letters*, 389, 143–154. doi: 10.1016/j.epsl.2013.12.028
- 1329 Silver, P. G., Behn, M. D., Kelley, K., Schmitz, M., & Savage, B. (2006). Under-  
1330 standing cratonic flood basalts. *Earth and Planetary Science Letters*, 245(1-2),  
1331 190–201. doi: 10.1016/j.epsl.2006.01.050
- 1332 Sodoudi, F., Yuan, X., Kind, R., Lebedev, S., Adam, J. M., Kästle, E., & Tilmann,  
1333 F. (2013). Seismic evidence for stratification in composition and anisotropic fab-  
1334 ric within the thick lithosphere of Kalahari Craton. *Geochemistry, Geophysics,*  
1335 *Geosystems*, 14(12), 5393–5412. doi: 10.1002/2013GC004955
- 1336 Sparks, R., Baker, L., Brown, R., Field, M., Schumacher, J., Stripp, G., & Walters,  
1337 A. (2006). Dynamical constraints on kimberlite volcanism. *Journal of Volcanology*  
1338 *and Geothermal Research*, 155(1-2), 18–48.
- 1339 Stagno, V., Cerantola, V., Aulbach, S., Lobanov, S., McCammon, C. A., & Merlini,  
1340 M. (2019). Carbon-bearing phases throughout earth’s interior. In *Deep carbon:*  
1341 *Past to present* (pp. 66–88). Cambridge University Press.
- 1342 Sun, C., & Dasgupta, R. (2020). Thermobarometry of CO<sub>2</sub>-rich, silica-  
1343 undersaturated melts constrains cratonic lithosphere thinning through time in  
1344 areas of kimberlitic magmatism. *Earth and Planetary Science Letters*, 550,  
1345 116549. doi: 10.1016/j.epsl.2020.116549
- 1346 Sun, W., Jiang, J., Dai, L., Hu, H., Wang, M., Qi, Y., & Li, H. (2021). Electrical  
1347 properties of dry polycrystalline olivine mixed with various chromite contents:  
1348 Implications for the high conductivity anomalies in subduction zones. *Geoscience*  
1349 *Frontiers*, 101178.

- 1350 Svensen, H., Corfu, F., Polteau, S., Hammer, Ø., & Planke, S. (2012). Rapid magma  
1351 emplacement in the Karoo Large Igneous Province. *Earth and Planetary Science*  
1352 *Letters*, *325-326*, 1–9. doi: 10.1016/j.epsl.2012.01.015
- 1353 Van Achterbergh, E., Griffin, W. L., & Stiefenhofer, J. (2001). Metasomatism  
1354 in mantle xenoliths from the Letlhakane kimberlites: Estimation of element  
1355 fluxes. *Contributions to Mineralogy and Petrology*, *141*(4), 397–414. doi:  
1356 10.1007/s004100000236
- 1357 Van Schijndel, V., Cornell, D. H., Frei, D., Simonsen, S. L., & Whitehouse, M. J.  
1358 (2014). Crustal evolution of the rehoboth province from archaean to mesoprotero-  
1359 zoic times: Insights from the rehoboth basement inlier. *Precambrian Research*,  
1360 *240*, 22–36. doi: 10.1016/j.precamres.2013.10.014
- 1361 VanTongeren, J. A. (2017). *Mixing and unmixing in the bushveld complex magma*  
1362 *chamber*. Elsevier Inc. doi: 10.1016/B978-0-12-811159-8.00005-6
- 1363 Wang, D., Karato, S. I., & Jiang, Z. (2013). An experimental study of the influ-  
1364 ence of graphite on the electrical conductivity of olivine aggregates. *Geophysical*  
1365 *Research Letters*, *40*(10), 2028–2032. doi: 10.1002/grl.50471
- 1366 Wang, D., Mookherjee, M., Xu, Y., & Karato, S. I. (2006). The effect of water on  
1367 the electrical conductivity of olivine. *Nature*, *443*(7114), 977–980. doi: 10.1038/  
1368 nature05256
- 1369 Watson, H. C., Roberts, J. J., & Tyburczy, J. A. (2010). Effect of conductive im-  
1370 purities on electrical conductivity in polycrystalline olivine. *Geophysical Research*  
1371 *Letters*, *37*(1), 1–6. doi: 10.1029/2009GL041566
- 1372 Webb, S. J., Ashwal, L. D., & Cawthorn, R. G. (2011). Continuity between east-  
1373 ern and western Bushveld Complex, South Africa, confirmed by xenoliths from  
1374 kimberlite. *Contributions to Mineralogy and Petrology*, *162*(1), 101–107. doi:  
1375 10.1007/s00410-010-0586-z
- 1376 Weckmann, U. (2012). Making and Breaking of a Continent: Following the Scent of  
1377 Geodynamic Imprints on the African Continent Using Electromagnetics. *Surveys*  
1378 *in Geophysics*, *33*(1), 107–134. doi: 10.1007/s10712-011-9147-x
- 1379 White-Gaynor, A. L., Nyblade, A. A., Durrheim, R., Raveloson, R., van der Mei-  
1380 jde, M., Fadel, I., ... Sitali, M. (2020). Lithospheric Boundaries and Up-  
1381 per Mantle Structure Beneath Southern Africa Imaged by P and S Wave Ve-  
1382 locity Models. *Geochemistry, Geophysics, Geosystems*, *21*(10), 1–20. doi:  
1383 10.1029/2020GC008925
- 1384 Withers, A. C., Bureau, H., Raepsaet, C., & Hirschmann, M. M. (2012). Calibra-  
1385 tion of infrared spectroscopy by elastic recoil detection analysis of H in synthetic  
1386 olivine. *Chemical Geology*, *334*, 92–98. doi: 10.1016/j.chemgeo.2012.10.002
- 1387 Yang, Y., Li, A., & Ritzwoller, M. H. (2008). Crustal and uppermost man-  
1388 tle structure in southern Africa revealed from ambient noise and teleseis-  
1389 mic tomography. *Geophysical Journal International*, *174*(1), 235–248. doi:  
1390 10.1111/j.1365-246X.2008.03779.x
- 1391 Yousof, M., Thybo, H., Artemieva, I. M., & Levander, A. (2013). Moho depth and  
1392 crustal composition in Southern Africa. *Tectonophysics*, *609*, 267–287. doi: 10  
1393 .1016/j.tecto.2013.09.001
- 1394 Yousof, M., Thybo, H., Artemieva, I. M., & Levander, A. (2015). Upper mantle  
1395 structure beneath southern African cratons from seismic finite-frequency P- and  
1396 S-body wave tomography. *Earth and Planetary Science Letters*, *420*, 174–186. doi:  
1397 10.1016/j.epsl.2015.01.034
- 1398 Zeh, A., Ovtcharova, M., Wilson, A. H., & Schaltegger, U. (2015). The Bushveld  
1399 Complex was emplaced and cooled in less than one million years - results of zir-  
1400 conology, and geotectonic implications. *Earth and Planetary Science Letters*, *418*,  
1401 103–114. doi: 10.1016/j.epsl.2015.02.035
- 1402 Zeh, A., Wilson, A. H., & Gerdes, A. (2020). Zircon U-Pb-Hf isotope systematics  
1403 of Transvaal Supergroup – Constraints for the geodynamic evolution of the Kaap-

- 1404 vaal Craton and its hinterland between 2.65 and 2.06 Ga. *Precambrian Research*,  
1405 345(May), 105760. doi: 10.1016/j.precamres.2020.105760
- 1406 Zhang, B., & Yoshino, T. (2017, jan). Effect of graphite on the electrical conductiv-  
1407 ity of the lithospheric mantle. *Geochemistry, Geophysics, Geosystems*, 18(1), 23–  
1408 40. doi: 10.1002/2016GC006530
- 1409 Zhang, B., Yoshino, T., Wu, X., Matsuzaki, T., Shan, S., & Katsura, T. (2012).  
1410 Electrical conductivity of enstatite as a function of water content: Implications for  
1411 the electrical structure in the upper mantle. *Earth and Planetary Science Letters*,  
1412 357-358, 11–20.
- 1413 Zirakparvar, N. A., Mathez, E. A., Scoates, J. S., & Wall, C. J. (2014). Zircon  
1414 Hf isotope evidence for an enriched mantle source for the Bushveld Igneous  
1415 Complex. *Contributions to Mineralogy and Petrology*, 168(3), 1–18. doi:  
1416 10.1007/s00410-014-1050-2